

**Morphology is a Link to the Past: examining formative
and secular galactic evolution through morphology**

**A THESIS
SUBMITTED TO THE FACULTY OF THE GRADUATE SCHOOL
OF THE UNIVERSITY OF MINNESOTA
BY**

Melanie A. Galloway

**IN PARTIAL FULFILLMENT OF THE REQUIREMENTS
FOR THE DEGREE OF
Doctor of Philosophy**

**Advisor:
Lucy Fortson**

month, 2017

© Melanie A. Galloway 2017
ALL RIGHTS RESERVED

Acknowledgements

Some acknowledgements

Dedication

Firstly dedicated to Zuko, for being the sweetest little bird.

Abstract

Galaxy morphology is one of the primary keys to understanding a galaxy's evolutionary history. External mechanisms (environment/clustering, mergers) have a strong impact on formative evolution of the major galactic components (disk, bulge, Hubble type), while internal instabilities created by bars, spiral arms, or other substructures drive secular evolution via the rearrangement of material within the disk. This thesis will explore several ways in which morphology may impact the dynamics and evolution of a galaxy using visual classifications from several Galaxy Zoo projects. Section 1 will focus on the present morphology of galaxies in the local Universe ($z < 0.2$) using data from Galaxy Zoo 2 and Galaxy Zoo UKIDSS. Section 2 will examine populations of morphologies at various lookback times, from $z = 0$ out to $z = 1$ using data from Galaxy Zoo Hubble.

We first explore the impact of bars in disc galaxies on channeling gas from the outer regions of the disk to the inner few kpc necessary to fuel an active galactice nucleus (AGN). Using a sample of 19,756 disk galaxies at $0.01 < z < 0.05$ imaged by the Sloan Digital Sky Survey and morphologically classified by Galaxy Zoo 2, the difference in AGN fraction in barred and unbarred disks was measured. A weak, but statistically significant, effect was found in that the population of AGN hosts exhibited a 16.0% increase in bar fraction as compared to their unbarred counterparts at fixed mass and color. These results are consistent with a cosmological model in which bar-driving fueling contributes to the fueling of growing black holes, but other dynamical mechanisms must also play a significant role.

We study the wavelength dependence on morphology by comparing the optical morphological classifications from GZ2 to classifications done on infrared images in GZ:UKIDSS. We find some cool result. [to be continued]

We examine more directly the morphological changes in galaxy populations as a function of their age using classifications from Galaxy Zoo: Hubble. A sample of XX,XXX disc galaxies from the COSMOS field at $0 < z < 1$ were identified as active or passive using a NUV-r / r -J diagnostic with rest-frame colors from the UltraVISTA catalog. We find that the fraction of disks that are passive increases/decreases from X.X% at

$z = 1$ to X.X% at $z = 0$. We interpret this result as [something having to do with the transformation of disk to elliptical, depending on result]. Additionally, we emphasize the challenges of visual classification that are particular to galaxies at high redshift. We present a correction technique to address these biases using simulated images of nearby SDSS galaxies which were artificially redshifted using the FERENGI code and classified in GZH.

Contents

Acknowledgements	i
Dedication	ii
Abstract	iii
List of Tables	viii
List of Figures	ix
1 Introduction	1
1.1 Morphological Categorization of Galaxies	2
1.1.1 Ellipticals	2
1.1.2 Spirals	4
1.1.3 Lenticulars/S0s	4
1.2 Morphology as a tracer of galaxy evolution	5
1.2.1 Color-Morphology Bimodality	5
1.2.2 Morphology and Stellar populations	6
1.2.3 Morphology and Environment	6
1.2.4 Bars	8
1.3 Methods for morphological classification	10
2 Methodology	12
2.1 A Brief History of Galaxy Zoo	12
2.2 Galaxy Zoo Data Reduction	14

2.2.1	User weighting by consistency	14
2.2.2	Classification bias in the local Universe	17
3	Bar AGN project	22
4	UKIDSS	23
4.1	Intro: wavelength dependence on morphology: optical and IR	23
4.2	UKIDSS sample	26
4.2.1	S/N method for selecting equally-sized galaxies	28
4.3	Comparison of Hubble Types in Spirals	32
4.4	Bar Fraction	37
5	Using FERENGI to correct f_{features} for redshift-induced classification bias	44
5.1	Intro	44
5.1.1	The FERENGI code	45
5.2	The FERENGI sample	48
5.3	Measuring the drop in f_{features} as a function of z and μ using FERENGI data	50
5.3.1	Identifying “correctable” and “lower limit” samples.	50
5.3.2	Computing debiased f_{features} for the “correctable” sample using the ζ equation	55
5.3.3	Results and the NEI sample: limitations of the FERENGI simulated data	56
5.4	Ferengi 2: using simulated images to measure incompleteness in disk fraction as a function of redshift and surface brightness	59
5.4.1	The Ferengi 2 Sample	61
6	GZH red disk fraction	66
6.0.2	Quenching Mechanisms	68
6.1	Sample Selection	70
6.2	Galaxy Classification: Identifying the Passive Population	70
6.3	Using Ferengi2 to correct for incompleteness in the red disk fraction	71

List of Tables

4.1	Comparison of depth and resolution of the UKDISS and GZ2 images. The resolution between the two surveys is comparable, but the UKIDSS images are an average of ~ 1 magnitude shallower in all bands used to create the color-composite images that were classified.	27
5.1	Number of correctable galaxies for the top-level task in GZH, split by <i>HST</i> survey.	55

List of Figures

1.1	The Hubble Tuning fork with gri-composite SDSS images as examples of the various types. Credit: Karen Masters and The Sloan Digital Sky Survey (SDSS) Collaboration.	3
1.2	Color vs. Absolute Magnitude Diagram, illustrated using SDSS galaxies. In each color-magnitude bin, a random galaxy was selected meeting the criteria defined by that bin.	7
1.3	Credit: Buta (2013), Figure 2.51. Spiral galaxy M51 observed in optical B-band (left), near-IR (middle), and mid-IR (right). Visible in the B-band image are patchy regions of star-formation and dust lanes, which become invisible in the near-IR, giving an overall smoother appearance. The mid-IR image shows regions where the dust re-radiates light absorbed from star-forming regions, giving a similar appearance to the optical image.	8
2.1	GZ1Interface	14
2.2	Interface	15
2.3	Decision tree used in the Galaxy Zoo:Hubble project. The colors indicate the “Tier” level of the question. Gray represents 1st-Tier; these are asked of all users. Green are 2nd-Tier; these are only asked after responding to a 1st-Tier question, and so on. This tree is identical to GZ2 and UKIDSS, except for the addition of the clumpy questions T12-T18.	16
2.4	Local ratios of morphologies for the first three tasks in the GZ2 decision tree, used to derive debiased votes for the GZ2 sample. The full figure which includes baseline ratios for all tasks in the GZ2 decision tree is shown in Willett et al. (2013), Figure 5.	18

2.5 Placeholder - will make original later. Shows results of 2 debiasing methods for the first 3 tasks in GZ2	19
2.6 Placeholder - make my own later. Left shows how voronoi binning is done; compare to rectangular binning in W13. Right is cumulative distribution of some vote fraction at low and high redshift.	21
4.1 Examples of two galaxies whose morphological changes between optical and IR wavelengths was driven by a lack of light detectable in the IR relative to optical. Top: A galaxy classified as featured and spiral in the optical using GZ2 vote fractions, but smooth in the IR using UKIDSS vote fractions (dr7objid: 587726014553587781). Bottom A galaxy classified as featured and barred in the optical using GZ2 vote fractions, but due to the complete disappearance of arms in the IR, only the bar is visible, giving it the appearance and classification of an edge-on galaxy (dr7objid: 587734305416871963)	29
4.2 Example of the $r_3^J/r_{2\text{petro}}^r$ calculation of one galaxy (dr7objid=587722981747392587). Top Left: The sky-subtracted background of the J-band images are fit to a Gaussian to derive the noise N , which is given as the standard deviation of the fit. Top right: The signal to noise profiles of the J-band images. The radius at which the signal-to-noise falls below three is indicated by the green dashed line, and the threshold $S/N = 3$ is indicated by the horizontal black dashed line. The blue line shows twice the r-band petrosian radius $r_{2\text{petro}}^r$ for comparison. Bottom: Color-composite of the optical gri image (left) and IR YJK image (right). The dashed circles represent the radius $r_{2\text{petro}}^r$ (left) and r_3^J (right), derived as shown in the top row. The ratio of the two radii is given, showing that for this galaxy, the light in the IR image extends to 62% of the optical image.	31
4.3 Example optical gri (left) and IR YJK (right) images of galaxies, sorted by $r_3^J/r_{2\text{petro}}^r$. The circle on the optical image (left) shows $r_{2\text{petro}}^r$, and circle on the IR image (right) shows the J-band radius within which $(S/N)_J > 3$, r_3^J	32

4.4	The change in GZ2 and UKIDSS vote fractions is strongest at low values of $r_3^J/r_{2\text{petro}}^r$, where the light detectable in the J-band extends to a significantly smaller area than than the r-band images. Left: Distribution of the change in f_{features} from GZ2 to UKIDSS as a function of $r_3^J/r_{2\text{petro}}^r$. Right: The average change in f_{features} from GZ2 to UKIDSS as a function of $r_3^J/r_{2\text{petro}}^r$. The shaded region indicates the $1-\sigma$ dispersion around the mean. The dashed line at $r_3^J/r_{2\text{petro}}^r = 0.75$ indicates the threshold below which galaxies are excluded from the comparison sample, due to the coverage of light in the J-band not reaching a significant area as represented in the r-band.	33
4.5	IR images of galaxies tend to have a looser appearance of arms and more prominent bulges than in optical images. Shown is the difference between optical and IR $f_{\text{tight arms}}$ as a function of optical/GZ2 $f_{\text{tight arms}}$ (left), and difference between optical and IR $f_{\text{obv+dom}}$ as a function of optical/GZ2 $f_{\text{obv+dom}}$ (right) for 502 galaxies which were classified as spiral in both IR and optical images. The colors represent the fraction of galaxies that populate any given bin, and bins which could not represent a possible difference in vote fraction ($\Delta f > f$ or $\Delta f < f - 1$) are colored black. The blue dotted line in both represents a difference in vote fraction of 0, such that galaxies above the line have larger IR vote fractions for the feature represented in each plot, respectively.	35
4.6	Flow diagram showing the breakdown of morphologies in the UKIDSS sample. Left: 15,491 galaxies in the volume-limited sample. Right: 2,346 SONIs: galaxies which were classified as spiral in the optical GZ2 classifications but do not follow the spiral path in the UKIDSS classifications.	38
4.7	Example images of galaxies which were classified as spiral in optical GZ2 classifications but followed the “smooth” path in the UKIDSS classifications.	39
4.8	Example images of galaxies which were classified as spiral in optical GZ2 classifications but followed the “featured, not edge-on, no spiral” path in the UKIDSS classifications.	39

4.9	Example images of galaxies which were classified as spiral in optical GZ2 classifications but followed the “featured, edge-on” path in the UKIDSS classifications.	40
4.10	Example images of galaxies which were classified as spiral in optical GZ2 classifications but were classified as star/artifact in the UKIDSS classifications.	40
4.11	Dotted lines indicate the threshold for bar classification; $f_{bar} > 0.3$. Galaxies shown had at least 20 people answering the bar question.	41
4.12	Galaxies classified as barred in optical GZ2 and unbarred in infrared UKIDSS.	42
4.13	Galaxies classified as barred in infrared UKIDSS and unbarred in optical GZ2.	43
5.1	Examples of two SDSS galaxies which have been run through the FERENGI code to produce simulated <i>HST</i> images. The measured value of f_{features} from GZH for the images in each panel are (1) Top row: $f_{\text{features}} = (0.900, 0.625, 0.350, 0.350, 0.225)$ and (2) Bottom row: $f_{\text{features}} = (1.000, 0.875, 0.875, 0.625, 0.375)$	49
5.2	Effects of redshift bias in 3,449 images in the FERENGI sample. Each point <i>in a given redshift and surface brightness bin</i> represents a unique galaxy. On the y -axis in each bin is the f_{features} value of the image of that galaxy redshifted to the value corresponding to that redshift bin. On the x -axis is the f_{features} value of the image of the same galaxy redshifted to $z = 0.3$. The dashed black lines represent the best-fit polynomials to the data in each square. The solid black line represents $f_{\text{features},z=f_{\text{features}},z=0.3}$. Regions in which there is a single-valued relationship between f_{features} at high redshift and at $z = 0.3$ are white; those in which there is not are blue, and those with not enough data ($N < 5$) are grey. A larger version of the bin outlined at $z = 1.0$ and $20.3 < \mu < 21.0$ (mag/arcsec 2) is shown in Figure 5.3.	51

5.3	A larger version of the dark-outlined square in Figure 5.2, containing FERENGI galaxies that have been artificially redshifted to $z = 1.0$ and have surface brightnesses between $20.3 < \mu < 21.0$ (mag/arcsec 2). The orange bars represent the inner 68% (1σ) of the uncorrectable f_{features} quantiles, which are used to compute the limits on the range of debiased values.	52
5.4	The final separation of the correctable and lower-limit samples in redshift/surface brightness/ f_{features} space. Pink points are all FERENGI galaxies in the unshaded regions of Figure 5.2. Blue points are all FERENGI galaxies in the blue shaded regions of Figure 5.2. The solid black line is the convex hull which encloses the uncorrectable points and defines the region of the lower-limit sample.	54
5.5	Behaviour of the normalised, weighted vote fractions of features visible in a galaxy (f_{features}) as a function of redshift in the artificial FERENGI images. Galaxies in this plot were randomly selected from a distribution with evolutionary correction $e = 0$ and at least three detectable images in redshift bins of $z \geq 0.3$. The displayed bins are sorted by $f_{\text{features},z=0.3}$, labeled above each plot. Measured vote fractions (blue solid line) are fit with an exponential function (red dashed line; Equation 5.4); the best-fit parameter for ζ is given above each plot.	57
5.6	All fits for the FERENGI galaxies of the vote fraction dropoff parameter ζ for f_{features} as a function of surface brightness. This includes only the simulated galaxies with a bounded range on the dropoff ($-10 < \zeta < 10$) and sufficient points to fit each function (28 original galaxies, each with varying images artificially redshifted in one to eight bins over a range from $0.3 \lesssim z_{\text{sim}} \lesssim 1.0$).	58
5.7	Histogram showing the fraction of galaxies that have a finite correction for the debiased vote fractions $f_{\text{features,debiased}}$ as a function of f_{features} and redshift. The parameter space for corrections is limited to $0.3 \leq z \leq 1.0$ due to the sampling of the parent SDSS galaxies and detectability in the FERENGI images.	59

5.8	Surface brightness as a function of redshift for 3,449 FERENGI images and the 102,548 <code>main</code> galaxies with measured μ and z values. The colour histogram shows the number of FERENGI images as a function of μ and z_{sim} . White contours show counts for the galaxies in the <code>main</code> sample, with the outermost contour starting at $N = 1500$ and separated by intervals of 1500.	60
5.9	Example of a galaxy overlapping the edge of the SDSS frame. Shown is the bulk r-band fits image for SDSS DR12 run 3903, camcol 6, and field 60. The boxed-in galaxy (SDSS DR12 objid 1237662239079268544) is too close to the edge of the image to create a cutout that encloses the entire galaxy. The pink dashed box indicates a cutout size of $2^*\text{PETRO}R90_R$, the blue solid line indicates a cutout size of $2.5^*\text{PETRO}R90_R$	63
5.10	Examples of two galaxies whose minimum simulated redshifts in FERENGI were larger than $z_{\text{sim}} = 0.3$. These were detected via visual inspection and removed from the final FERENGI2 sample.	64
5.11	Examples of FERENGI2 galaxies. The left is the original gri-composite image of the source galaxy. Images on the right are simulated output from the FERENGI code. Only four of the eight simulated redshifts are shown in the interest of space.	65
6.1	cmd figure	67
6.2	Evolution of colors using stellar population synthesis models. Galaxy was assumed to have formed at $z = 6$ for plotting purposes.	71
6.3	Separation of the quiescent population (red sequence) and active population (blue cloud) of the FERENGI2 sample.	73

6.4 Example calculation of completeness ξ at redshift $z = 0.7$. Points represent FERENGI2 images classified in Galaxy Zoo. The y-axis corresponds to the value of f_{features} measured at the galaxy redshifted to $z = 0.7$, and the x-axis corresponds to the value of f_{features} measured at the galaxy redshifted to $z = 0.3$. On average, the f_{features} is lower at the higher redshift, indicating users on average have more difficulty identifying features in images at higher redshifts. The dotted lines correspond to $f_{\text{features}}=0.3$, the threshold above which a galaxy is considered to have a disk. Galaxies to the right of the vertical dashed line were identified as disks at the lowest redshift $z = 0.3$, the total number defined as N_{true} , the true number of disks. Galaxies above the horizontal dash line were identified as disks at the higher redshift $z = 0.7$, the total number defined as N_{detected} . The ratio $\xi = N_{\text{detected}}/N_{\text{true}}$ is the completeness value; in this example, only 61% of disks were detected at $z = 0.7$.	75
6.5 Completeness ξ as a function of redshift and surface brightness for red sequence (left) and blue cloud galaxies (right).	76
6.6 Completeness ξ as a function of redshift and surface brightness for red sequence (left) and blue cloud galaxies (right).	77
6.7 Completeness ξ as a function of redshift moneypot	78

Chapter 1

Introduction

The clues to galaxy formation and evolution are hidden in the fine details of galaxy structure.

Peng et al., 2002

The processes which govern the formation, growth, and death of galaxies are difficult to track. We cannot observe a galaxy from its birth to its death, all we have available is a single snapshot of the Universe. We must rely on other tools to map out the history of a galaxy's complete evolution.

Morphology is one of the most powerful tools for revealing the physical processes that shape the evolution of galaxies. Details of a galaxy's structure are known to be linked with its color (), recent star-formation (), merger history (), and black hole activity (), among others. There is no debate today that morphology is strongly linked to galactic evolution, but the extent to which these relationships hold is still difficult to quantify. Morphological classifications on scales large enough for results to claim statistical significance have been, in the past, unavailable. While expert visual classifications succeeded in accuracy, they lacked in numbers; the opposite has been true for computational methods.

This research examines the link between morphology and evolution using data from the Galaxy Zoo project, which uses crowd-sourcing to provide a “best-of-both-worlds”

approach to morphological classifications. To date, over X million volunteers have identified the structures of over Y million galaxies, providing the benefits of both visual inspection and large numbers. With these data, the ways in which morphology drives (or is driven by) a galaxy’s evolution has been investigated on a scale previously unachievable.

1.1 Morphological Categorization of Galaxies

The oldest and most well-known system which categorizes galaxies based on their structure was developed by Edwin Hubble, commonly known as the “Hubble Tuning-Fork” (Hubble, 1926). Using a small sample of photometric images of nearby galaxies, Hubble identified two fundamental morphological classes: spirals, which exhibited well-defined disk structure and clear spiral arms, and ellipticals, whose light distributions were smoothed over a roughly spherical shape. Only 3% of the sample had structures which deviated from these two categories, showing no evidence of rotational symmetry about a dominating nucleus; these were grouped together and labeled “Irregular”. Although Hubble’s system was originally based on a mere 400 galaxies, the classifications are still valid for describing the morphologies of the millions of galaxies identifiable today (albeit with some modifications, ie. DeVaucouleur’s revised system (de Vaucouleurs, 1963)).

An example of Hubble’s Tuning Fork is shown in Figure 1.1. The classifications defined on the Tuning Fork are as follows:

1.1.1 Ellipticals

The left side of the tuning fork contains elliptical galaxies, labeled “E”. These were originally identified as circular through flattened ellipses whose luminosity faded smoothly from the center to “indefinite edges.” The only other structural feature evident to subdivide this class were their ellipticities, defined in the traditional way $e = (a - b)/a$. A number is added to the label that represents the ellipticity, with the decimal omitted, whereby E0 would represent a purely spherical elliptical ($e = 0$), and E7 being the most elongated ($e = 0.7$). Hubble assumed that any galaxy with an ellipticity higher than 0.7 was no longer an elliptical, but more likely a highly-inclined spiral. It should be noted

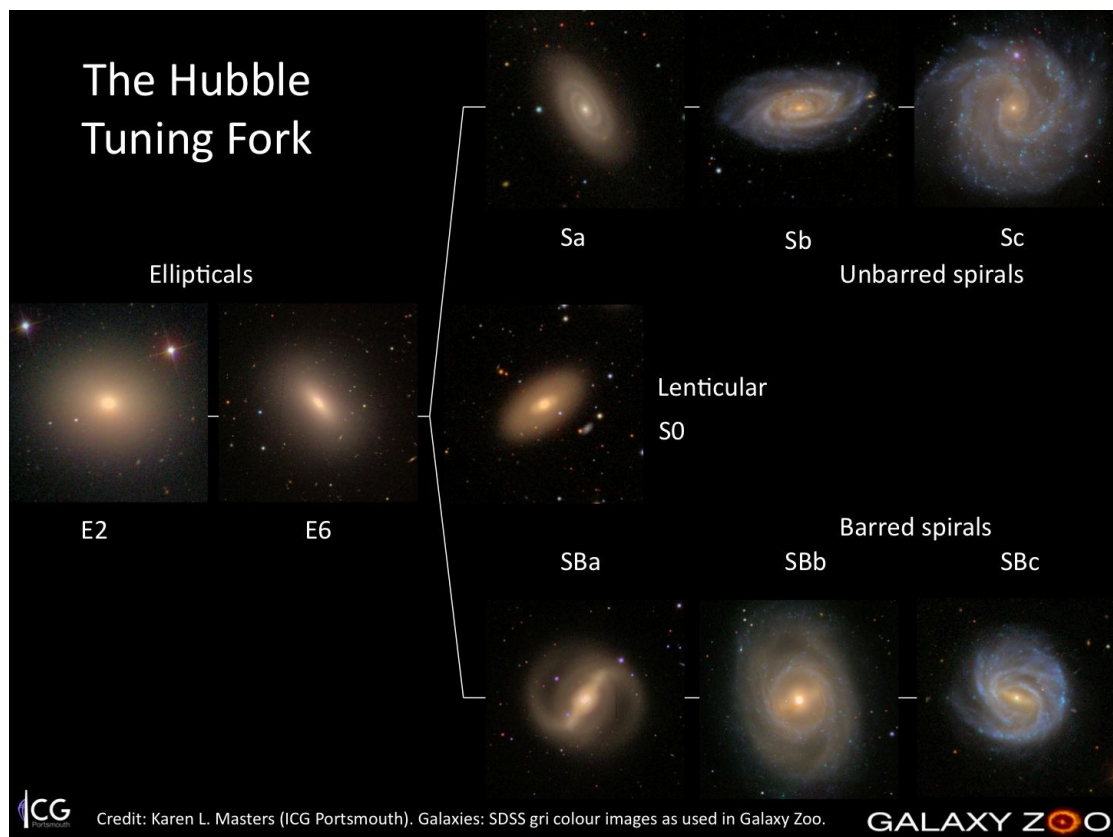


Figure 1.1 The Hubble Tuning fork with gri-composite SDSS images as examples of the various types. Credit: Karen Masters and The Sloan Digital Sky Survey (SDSS) Collaboration.

that these labels only classify the *projected* appearance; since ellipticals are tri-axial structures, this classification system is very dependent on the orientation angle of any ellipticals which are not perfectly spherical.

1.1.2 Spirals

The right side of the fork contains the various types of spiral galaxies. These all share the feature of having a flattened disk-shape, and tend to have a spherical bulge of stars in the center with spiral arms extending outward. Spirals whose arms originate from the central bulge follow the top of the fork, labeled “S”, while those whose arms originate at the ends of a central galactic bar follow the bottom, labeled “SB”. Both types are further classified based on the relative size of the central bulge and tightness of the arms. Those with large bulges and tighter arms are designated with an “a” attached to the spiral symbols, or “b”-“d” for decreasing bulge sizes and looser appearance of arms.

1.1.3 Lenticulars/S0s

Lenticular galaxies are placed at the center of the tuning fork, originally thought to be a transition stage to link the elliptical and spiral types. They exhibit the same overall disk-shape as the spirals, but have a smooth appearance rather than defined arms (which can make them difficult to distinguish from true ellipticals). They may or may not contain a galactic bar, giving them Hubble-type classifications of S0 (unbarred) or S0B (barred).

Hubble originally referred to the galaxies toward the left and right on the fork as “early” or “late”-type, respectively, simply for convenience in describing their relative positions on the sequence. While it is noted in his 1926 paper that any temporal connotation should be disregarded, the terms remain misleading in that it is now well-known that the early types tend to have older stellar populations, and late-types tend to be very young in their evolution. Nevertheless, “early-type” and “late-type” are still today used interchangeably when referring to ellipticals/S0s and disks.

1.2 Morphology as a tracer of galaxy evolution

The previous section described the most common morphological types of galaxies observed in the Universe. At this point it may be relevant to question, why are there different types at all? Do the different shapes exhibit different evolutionary pathways, or is the snapshot we see of the distributions simply showing different stages of a track that all galaxies eventually follow? The answers to these questions aren't fully known; however, examining the relationships between the different morphological types and their dynamics can provide strong insights to the full picture. This section will provide some examples of well-known links between morphology and galaxies' evolutionary histories.

1.2.1 Color-Morphology Bimodality

The color of a galaxy is a strong indicator of its recent star formation history. In general, photometrically blue galaxies are in the process of forming new stars, emitting high energy blue light that is detected abundantly in short-wavelength filters. In contrast, galaxies which have ceased forming stars sometime in the past contribute most of their flux to long-wavelength filters, resulting in redder colors. Perhaps surprisingly, there is also a strong correlation between the color of a galaxy and its morphology. The majority of galaxies ($\sim 80\%$) have been shown out to $z \sim 1$ to follow this relationship: blue galaxies tend to be late-type spirals, and red galaxies tend to be early-type/elliptical (Tully, R.B., Mould, J.R., Aaronson, 1982; Strateva et al., 2001; Baldry et al., 2004; Conselice, 2006; Martin et al., 2007; Mignoli et al., 2009). An example is shown in Figure 1.2.1. The vertical axis tracks the $u - r$ color, such that higher values are “redder” and smaller values are “bluer”. Bluer galaxies tend to have more featured morphologies; spiral arms appear more flocculant and clumps of star formation are apparent, generating irregular shapes in the extreme cases. Redder galaxies begin to have a much more smoothed-out and symmetric appearance, encompassing both ellipticals and bulge-dominated lenticulars. Color has long been considered such a strong indicator of morphology that it has been often used as a proxy for morphology when large-scale visible inspection has not been practical (Cooray, 2005; Lee & Pen, 2007; Salimbeni et al., 2008; Simon et al., 2009). This link is strong evidence that the processes which drive both morphology

and the cessation of star formation are related in some way (Masters et al., 2010; Buta, 2013). This topic is explored in greater detail in Chapter 6.

1.2.2 Morphology and Stellar populations

At the most basic level, morphology is simply a tracer of the observed distribution of light in the galaxy, which in turn traces the distribution of stars, gas, and dust. All light is not emitted equally, however: gas and younger, Population I stars will emit more light in optical and UV wavelengths, while older Population II stars emit more strongly in the infrared. Since these populations may have very different light distributions, there is inherently some dependence on morphology with the wavelengths within which it's observed.

Morphologies observed in optical bands are sensitive to pockets of star-formation regions, but other features can be obscured due to dust extinction, particularly those comprised of older stellar populations (such as bars); these can give galaxies an overall “patchy” appearance. In contrast, they appear smoother in the near-IR, where the effects of dust extinction are reduced and the older stellar populations dominate. An interesting effect occurs as the observation wavelength moves into the mid-IR: here, dust tends to re-radiate the light absorbed from star-formation regions, re-creating the appearance of the optical-band morphology. There has been debate as to whether the optical and near-IR morphologies are de-coupled to the extent that two classification schemes, one for each wavelength range, is justified (e.g. Block & Puerari (1999)). Chapter 4 will examine the optical and near-IR morphologies measured by Galaxy Zoo to add to this debate, as well as investigate whether bars are in fact easier to identify in the near-IR.

1.2.3 Morphology and Environment

A galaxy's environment can also be a predictor of its morphology. The morphology-density relationship, first quantified by Dressler (1980), observes an abundance of elliptical/ early-type morphologies in denser environments (de Souza et al., 1982; Postman, M. Geller, 1984). Since the merger rate correlates with environment density, it could be suggested that early-types are often the by-products of mergers, as opposed to a stage

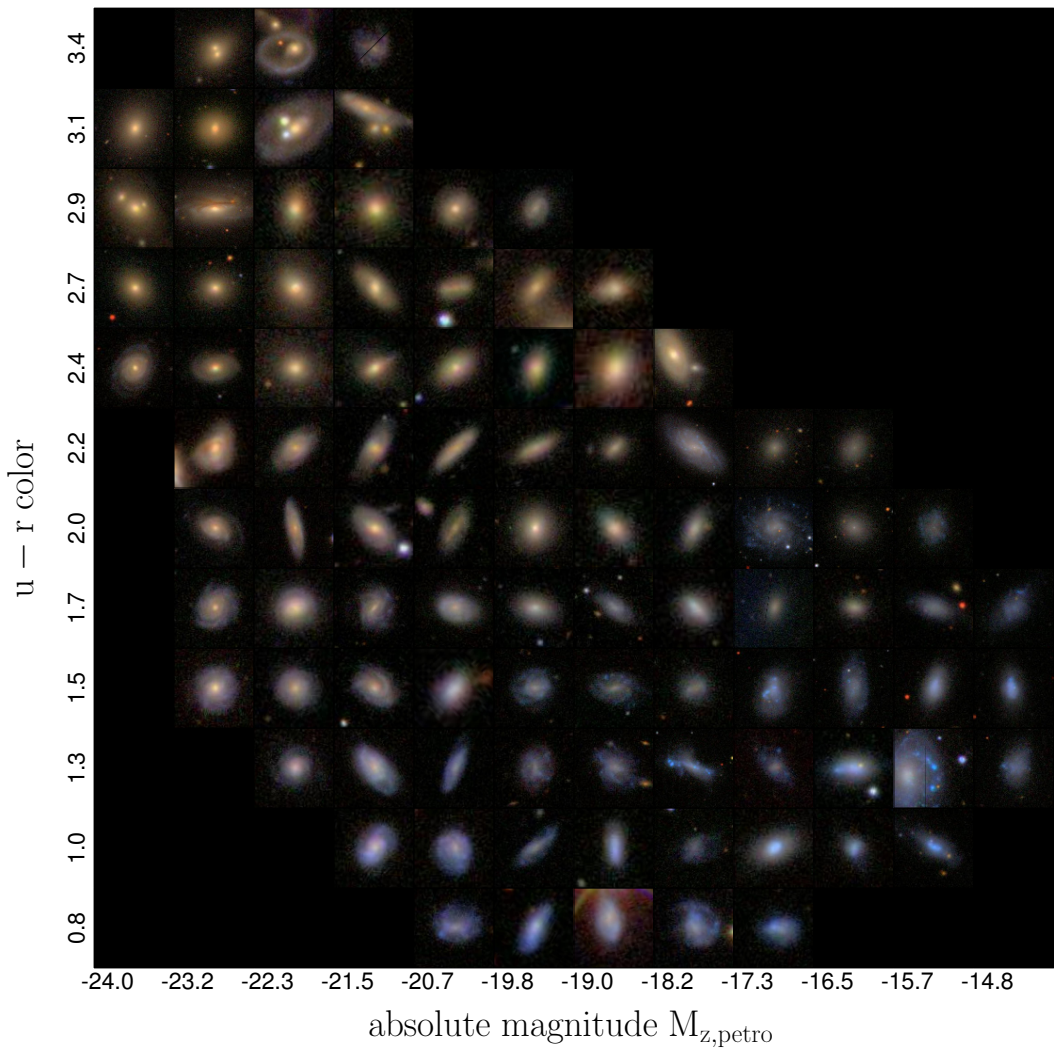


Figure 1.2 Color vs. Absolute Magntitude Diagram, illustrated using SDSS galaxies. In each color-magnitude bin, a random galaxy was selected meeting the criteria defined by that bin.

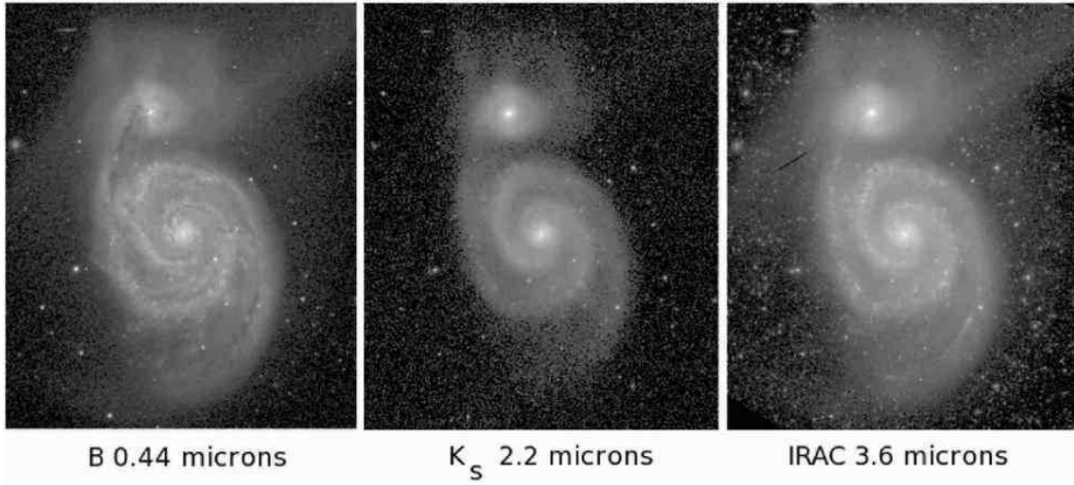


Figure 1.3 Credit: Buta (2013), Figure 2.51. Spiral galaxy M51 observed in optical B-band (left), near-IR (middle), and mid-IR (right). Visible in the B-band image are patchy regions of star-formation and dust lanes, which become invisible in the near-IR, giving an overall smoother appearance. The mid-IR image shows regions where the dust re-radiates light absorbed from star-forming regions, giving a similar appearance to the optical image.

of isolated secular evolution.

There is also evidence of an environmental impact on morphology even in the absence of direct merging. For example, ram pressure (Gunn & E. and Gott, III, 1972) exerted by the local intracluster medium can severely distort the gas distribution in a galaxy, resulting in asymmetries in the disk (ex. NGC 4402; see also Chapter 6).

1.2.4 Bars

Buta (2013) describes barred galaxies as “the ultimate in galaxy morphology.” His reasoning is simple: just by observing an image of a bar, it is easy to identify it as a major perturbation in an otherwise stable system. There is a great deal of truth in this; such a disruption will no doubt have significant effects on the fate of its host galaxy. In this way, bars are arguably one of the most important structural features that can shape a galaxy’s evolution.

A key feature of bars is their ability to drive gas from the outer regions of the galaxy to the center (Athanassoula, 1992; Friedli & Benz, 1993; Sellwood & Wilkinson, 1993;

Shlosman et al., 1989; Ann & Thakur, 2005), which can affect the galaxy's evolution in numerous ways. One such consequence is the formation of a pseudo-bulge Kormendy & Kennicutt (2004); Sheth et al. (2005). While this is seen in simulations, this theory is difficult to confirm observationally, as the bar may or not be destroyed by this process Athanassoula et al. (2005), causing difficulty in identifying a correlation between populations of galaxies with both bars and bulges.

An increased inflow of gas to the center may also increase central star-formation. Several studies have reported an increase in star-formation rates in the central region of barred galaxies vs. their unbarred counterparts (Hawarden et al., 1986; Ho et al., 1997), although this may only be true for strong bars. Martinet & Friedli (1997) and Zhou et al. (2014) find low rates of star-formation in galaxies with weak bars, suggesting they are unable to trigger significant star formation. Strong bars, however, show both the highest and lowest rates of star-formation. (Sheth et al., 2005) found a significant portion of barred galaxies with no molecular gas detected in the nuclear region, which may suggest that for these galaxies, the bar has already driven most of the gas to the nuclear region, where it was consumed by star-formation. Bars, then, seem to play two important roles in the star formation history of their host galaxies - both by increasing star formation, and subsequently driving the quenching process.

Bars also may be one of the mechanisms which enables the fueling of an active galactic nucleus (AGN), whose evolutions are believed to be strongly linked to that of their host galaxies (Schawinski et al., 2007, 2010; Antonini et al., 2015; Yang et al., 2017; Zubovas & Bourne, 2017) (and Heckman & Best (2014) for a comprehensive review). The requirements for onset of accretion onto the central SMBH are still unclear, but ? argues that non-axisymmetric components of the gravitational potential may be a necessary condition; a requirement which bars easily satisfy. While simulations have shown bars to provide the necessary inflow to ultimately fuel an AGN (Athanassoula, 1992; Friedli & Benz, 1993), observations have shown mixed results. Many have found an excess of AGN in barred samples of galaxies (Knapen et al., 2000; Oh et al., 2012), while others find no difference (Ho et al., 1997; Mulchaey & Regan, 1997; Cheung et al., 2015). A discussion of the discrepancies between these results, along with my own investigation of this topic, is the subject of Chapter 3.

The examples listed are only a few of the well-known relationships between the evolution of galaxies and their morphologies. There is little doubt amongst astronomers that morphology and galactic evolution are linked; however, as evident in these examples, some links are still inconclusive and the research of these relationships is still ongoing. Results are becoming more defined now, as methods to classify galaxies according to their morphologies are constantly improving. Some of the results listed from previous decades suffered from low-sample statistics, where it was only feasible to visually classify handfuls of galaxies in a single study. Today, more robust methods are able to categorize galaxies morphologically in a fraction of the time once required. The next section will explore the evolution of classification methods used to obtain galaxy morphologies for such studies.

1.3 Methods for morphological classification

Historically, most methods of morphological classification been done by visual inspection of small samples of images (e.g. Hubble (1926); Sandage (1961); de Vaucouleurs (1963); Block et al. (1994); Eskridge et al. (2002); Buta et al. (2010)), by either a single person or handful of experts. This method is becoming obsolete as we enter a new era of large data, with recent surveys such as SDSS and HST-Legacy, and upcoming JWST and LSST, producing high-quality images of hundreds of thousands of galaxies. To date, the largest morphological catalogs created by visual inspection from a small group of experts includes the Nair and Abraham catalog (Nair & Abraham, 2010) with $\sim 14,000$ galaxies, RC3 Catalog (de Vaucouleurs, 1991) with $\sim 23,000$ galaxies, and MOSES (Schawinski et al., 2007) with 50,000 galaxies. Even these catalogs, while successful, do not compare in size to the newly incoming data, and so more powerful and robust efforts are required to obtain morphological information on these scales.

One alternative to direct visual classification of morphologies is the use of proxies such as color, mass, surface brightness profile, or some combination of several. Color is commonly used as a proxy because of its mostly-tight relationship global morphology, in that spirals tend to be red and ellipticals tend to be blue. This type of morphological classification will always suffer from a high degree of inaccuracy, as there is no perfect physical measurement that is 100% correlated with shape. The morphology of a galaxy

traces the dynamical history, where proxies such as color trace stellar growth; these two properties thus reveal different evolutionary histories on possibly very different timescales Fortson et al. (2011). Last, while there are several proxies which correlate somewhat with the probability of a galaxy being spiral or elliptical, very few could be used to identify finer substructures or more detailed morphological features within the overall shape.

An ideal method for handling the large amounts of data would be an automated classification scheme. Several such algorithms have been developed, with some success (Odewahn et al., 2002; Peng et al., 2002; Conselice, 2003) by using the stellar light distribution of the galaxy to assign it a morphological class. These approaches tend to be limited to identifying the global morphologies (ie, spiral or elliptical), and lack the precision to accurately identify finer, detailed features (such as bars or the number of spiral arms) (Beck et al. 2017). Further, they tend to incorporate proxies such as color as their input, which are often not accurate as previously noted. Much more promising techniques are currently being tested which incorporate the use of machine-learning algorithms and neural networks (Dieleman et al., 2015; Huertas-Company et al., 2015),(Beck et al.2017), but these require massive and accurate training-sets to perform properly.

A best-of-both-worlds approach uses the power of crowdsourcing, which uses the input of thousands of individuals to visually classify galaxies in a fraction of the time achievable by a handful of experts; such a method was developed by Galaxy Zoo, the data from which is used throughout this thesis. The Galaxy Zoo project uses a simple online interface whereby images of galaxies are visually inspected by volunteers, which allows the identification of intricate morphological features to a higher degree of accuracy than computer algorithms today can achieve. Additionally, with a required 40+ independant classifications per galaxy, the resulting classifications carry a greater statistical significance than those generated from one or a few experts. The next chapter will describe how Galaxy Zoo collects data from volunteer citizen scientists, how the data is reduced and debiased, and finally how the data is used to assign morphological classifications to large samples of galaxies.

Chapter 2

Methodology

2.1 A Brief History of Galaxy Zoo

The increasing accessibility of the Internet in the last decade has allowed scientists to “outsource” tasks online using citizen science, with huge success. The project Seti@Home¹ (Anderson, 2002), launched in May 1999, was one of the first projects that revealed the massive number of people willing and excited to help contribute to science. Since launch, over 5 million participants donated idle time on their computers to assist SETI in analyzing radio telescope data to help in the search for extraterrestrial life. Citizen scientists were also extremely interested in taking an even more active role in research, as seen in a later project Stardust@Home², in which volunteers searched for dust grains in data via a web interface. This project engaged over 20,000 volunteers, and those who discovered dust grains were invited to become co-authors on the announcement papers. Early citizen science projects such as these inspired the launch of Galaxy Zoo.

The real need for a faster method of obtaining galaxy morphologies for large samples was realized in 2007 by graduate student Kevin Schawinski, who was studying populations of elliptical galaxies as work for his PhD thesis at Oxford University. At the time, the accepted and fastest method for identifying early-type galaxies (in large quantities) was to select based on SDSS-measured spectra (Bernardi et al., 2003). He

¹ <http://setiathome.berkeley.edu/>

² <http://stardustathome.ssl.berkeley.edu/>

knew, however, that this sort of method would exclude potential star-forming ellipticals (as well as potentially include passive spirals), due to the non-perfect correlation between morphology and color, as mentioned in the previous Chapter. So, realizing that a visual inspection of the direct appearance of the galaxies was necessary to create a complete sample of ellipticals independent of color, Schawinski devoted an entire week to classifying 50,000 galaxies by eye (MOSES, Schawinski et al. (2007)).

The grueling task of classifying only a small fraction of the entire SDSS main sample ($\sim 900,000$ galaxies) made it apparent that a better method for visual classification was becoming neccessary. Inspired by the 20,000 volunteers who participated in the Stardust@Home project, Schawinski and Oxford colleague Chris Lintott realized that it would only take a few years to classify all of SDSS Main, assuming a similar participation response as StarDust. This led to the launch of Galaxy Zoo in July, 2007. This first phase (known now as Galaxy Zoo 1, or GZ1), included the brightest (Petrosian magnitude $r < 17.77$ AB mag) 893,212 images from SDSS Data Release 6 (Strauss et al., 2002; AdelmanMcCarthy et al., 2008). In this project users were asked to indentify simple features of a given galaxy, including whether it was elliptical or spiral, clockwise or anticlockwise, a merger, or star/other (the original interface with options is shown in Figure 2.1).

In just the first day of the site being live, 20,000 classifications were coming in each hour - a rate much faster than the developers had ever expected. In less than a year, the entire SDSS main sample was classified by an average of 38 volunteers per galaxy. Following GZ1 data release paper published in April, 2008 (Lintott et al., 2008), over a dozen scienific publications were released which made use of the morphological classifications³. Significant results included the discovery of a large population of passive red spirals in the local universe (Masters et al., 2010), the existance of star-forming blue ellipticals (Schawinski et al., 2009b), “green peas,” a new class of galaxies exhibiting extremely high star formation (Cardamone et al., 2009), and “Hanny’s Voorwerp,” the first example of AGN-photoionized clouds detected near galaxies no longer actively hosting AGN (Lintott et al., 2009).

-Classifying galaxies by morphology *independently* of proxies like color or mass is important because the morphology traces the dynamics while color traces stellar content,

³ <https://www.zooniverse.org/about/publications>

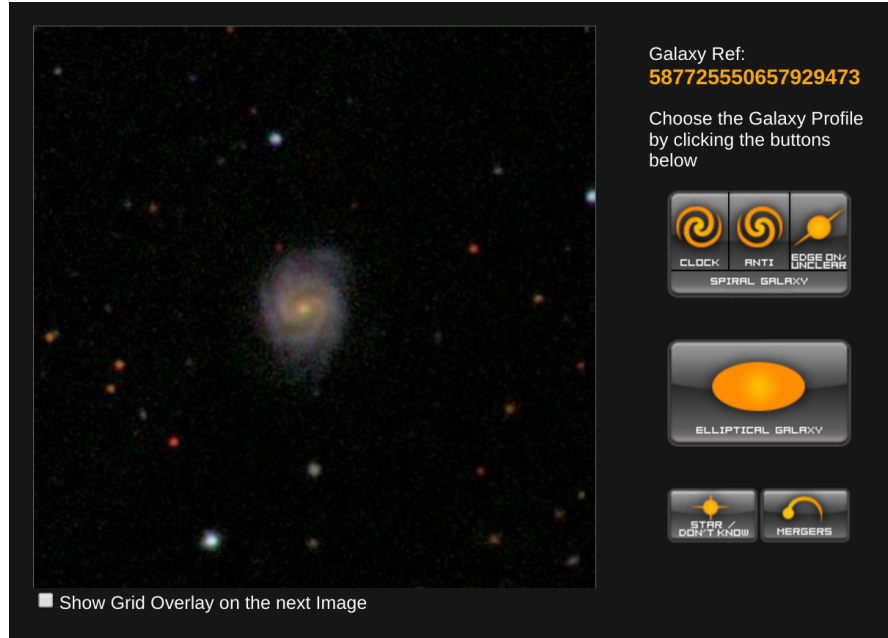


Figure 2.1 GZ1Interface

and these are only correlated on average and in the local universe. cite some motivations for crowdsourcing (ie Raddick; discussion of authentic scientific participation and learning)

2.2 Galaxy Zoo Data Reduction

2.2.1 User weighting by consistency

A typical Galaxy Zoo project collects classifications from over 10,000 unique volunteers. With such large numbers of classifiers, there exists the possibility that some fraction of these are “unreliable”, that is, their votes are consistent with random clicking. To ensure that all votes collected represent real classifications, a weighting technique is implemented to detect and down-weight unreliable votes.

The weighting scheme used for all GZ projects represented in this thesis (GZ2, GZ:UKIDSS, and GZ:Hubble) evaluates the consistency of each user by how often their votes agree with the majority for each task in the decision tree. The consistency rating κ for a single task is defined as:

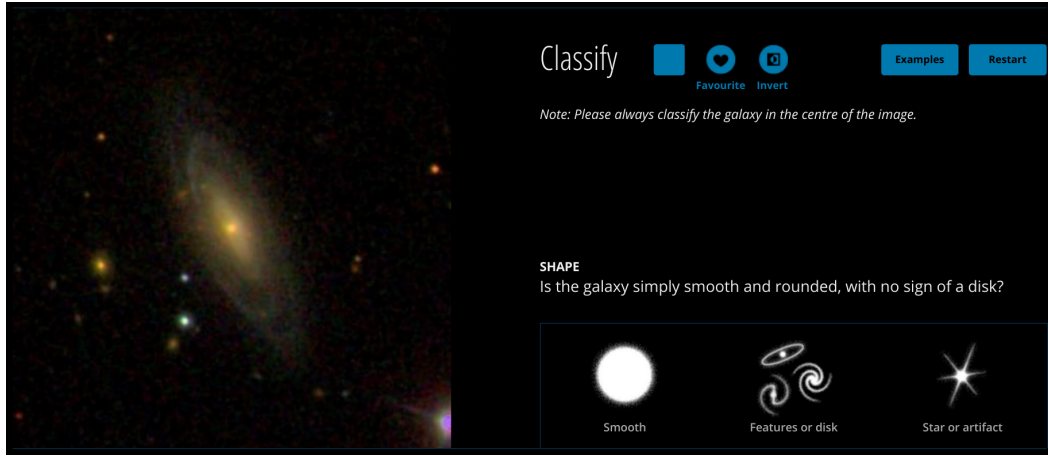


Figure 2.2 Interface

$$\kappa = \frac{1}{N_r} \sum_{i=1}^{N_r} \kappa_i \quad (2.1)$$

where f_r is the vote fraction for each response in the task, N_r represents the total number of responses to the task, $\kappa_i = f_r$ if the user's vote corresponds to response i , and $\kappa_i = (1 - f_r)$ if it does not. In this system, κ is then high if the vote agrees with the majority, and low if it does not.

The mean consistency computed for each response given is defined as the user's overall consistency $\bar{\kappa}$, and the user is assigned a weight w defined as:

$$w = \min(1.0, (\bar{\kappa}/0.6)^{8.5}) \quad (2.2)$$

All votes are then recalculated using the user weights, and the process is repeated as many as three times to ensure convergence. It can be seen in Equation 2.2 that a user's weight value is always less than or equal to one; in other words, users are only downweighted in cases of noticeable inconsistency, and never upweighted. Willett et al. (2013) show that most users with low consistencies tend to only have contributed a handful of classifications, which could either indicate that users become more accurate as they classify more galaxies, or that inconsistent users are inherently less likely to be interested in the project.

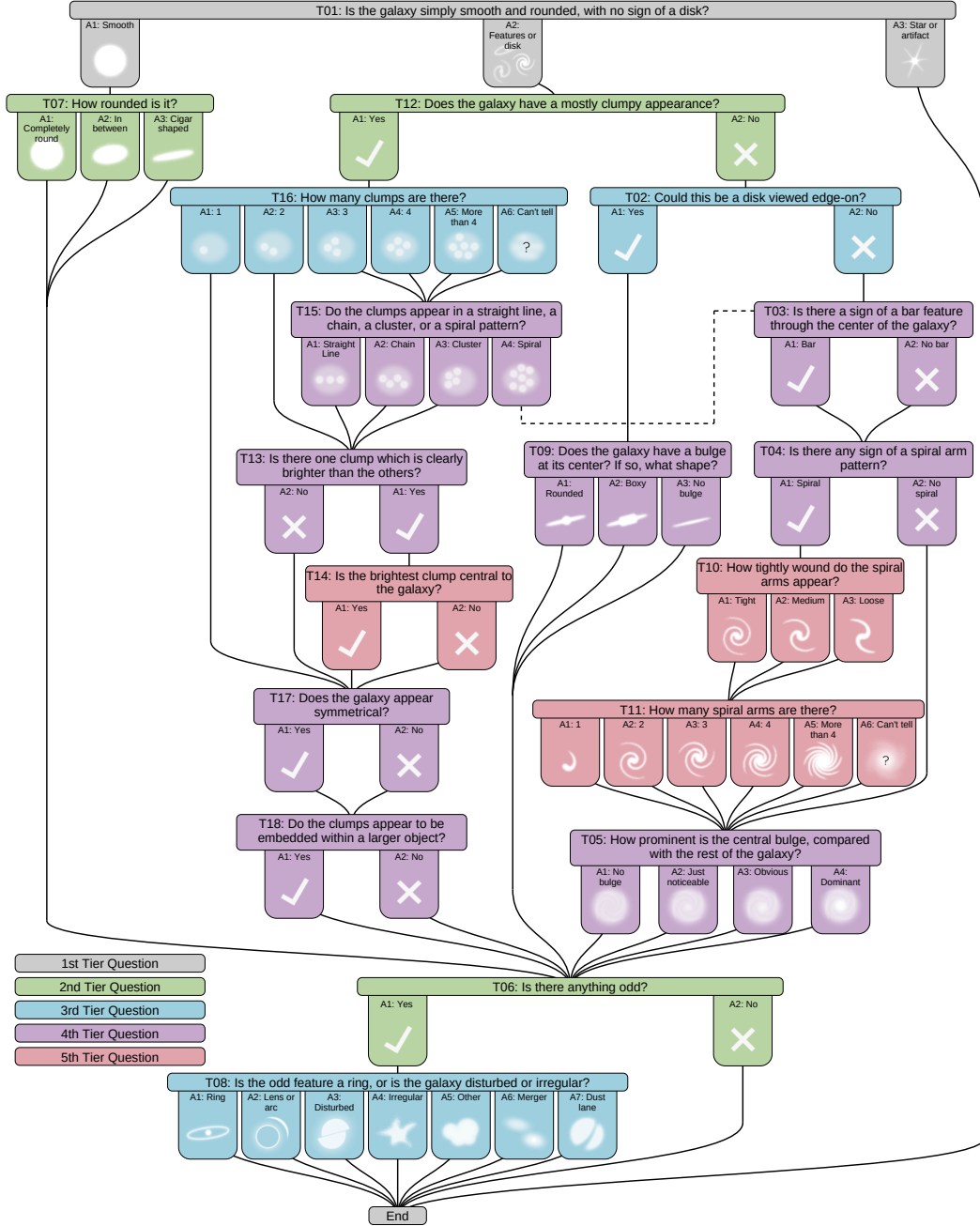


Figure 2.3 Decision tree used in the Galaxy Zoo:Hubble project. The colors indicate the “Tier” level of the question. Gray represents 1st-Tier; these are asked of all users. Green are 2nd-Tier; these are only asked after responding to a 1st-Tier question, and so on. This tree is identical to GZ2 and UKIDSS, except for the addition of the clumpy questions T12-T18.

2.2.2 Classification bias in the local Universe

For samples of galaxies limited to the local universe ($z \lesssim 0.2$), there is no expected redshift dependence on the morphological classifications. Therefore, we would expect vote fractions representing different morphological features to be constant with respect to redshift. However, this is not the case - the average vote fraction for features, bars, spirals, and several others actually tend to *decrease* with redshift. Since we assume such features should be equally prevalent at any redshift in this small range, some bias unrelated to any true morphological evolution must be affecting the vote fractions.

The source of this bias comes from the apparent size and brightness of the images of the galaxies being classified, which are strongly affected by redshift. Images of more distant galaxies appear smaller and dimmer, and therefore finer features are simply more difficult to detect. This sort of classification bias is a problem with any morphological classification, whether it be expert classifiers, automated detection, or crowd-sourced visual inspection.

This section will describe the methods used to correct this type of classification bias for galaxies in the local Universe, where no true morphological evolution is a factor. Beyond the local Universe this assumption is no longer valid, so techniques implementing classifications of artificially-redshifted galaxies are used for calibration; these are described in detail in Chapter ??.

Debiasing Galaxy Zoo 2: W13 method

The debiasing technique used in GZ2 assumed firstly that galaxies with similar brightnesses and sizes should, on average, share similar mixes of morphologies at any redshift. Using this assumption, galaxies were grouped into bins of absolute magnitude M_r , Petrosian effective radius R_{50} , and redshift. For each task in the GZ2 decision tree, the vote fractions for each response in any size/magnitude bin were adjusted so that their average matched the average vote fraction of its lowest-redshift bin. This method is described in detail in Willett et al. (2013), but the main approach is as follows:

For a given size/magnitude bin, the ratio of vote fractions for a pair of responses i and j for a single task can be written as f_i/f_j . Due to the classification bias described above, this ratio may not reflect the “true” ratio for this size/magnitude range, but can

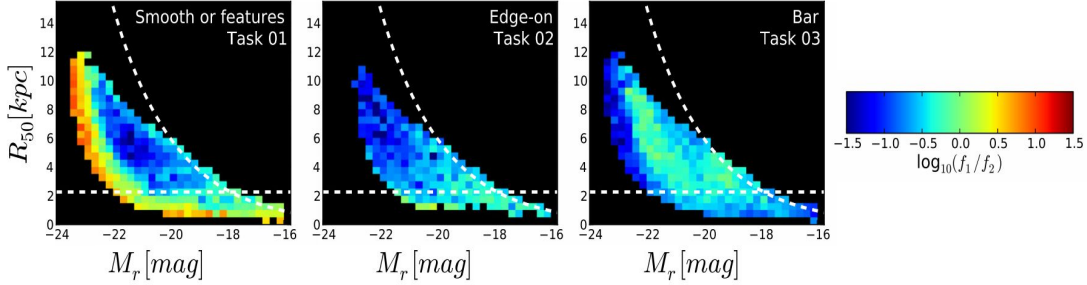


Figure 2.4 Local ratios of morphologies for the first three tasks in the GZ2 decision tree, used to derive debiased votes for the GZ2 sample. The full figure which includes baseline ratios for all tasks in the GZ2 decision tree is shown in Willett et al. (2013), Figure 5.

be written in terms of the true ratio with a multiplicative constant $K_{i,j}$:

$$\left(\frac{f_i}{f_j}\right)_{z=z'} = \left(\frac{f_i}{f_j}\right)_{z=0} \times K_{i,j} \quad (2.3)$$

Where $(f_i/f_j)_{z=z'}$ represents the ratio measured in a size/magnitude bin at $z = z'$, and $(f_i/f_j)_{z=0}$ is the “true,” or intrinsic ratio of vote fractions, defined as the ratio measured in the lowest redshift bin.

Figure 2.4 shows the local ($z = 0$) ratios of f_i/f_j for the first two responses i and j for the first three tasks of the GZ2 decision tree, which are used to calculate the debiased vote fractions as outlined above. For Task 01, f_i/f_j corresponds to $f_{smooth}/f_{features}$, for Task 02 $f_{edgeon}/f_{not\ edgeon}$, and for Task 03 $f_{bar}/f_{no\ bar}$. The figure demonstrates the size and magnitude dependence of the most local morphological populations: for example, in Task 01, the largest and brightest galaxies tend to have more votes for “smooth” than “featured”, which is consistent with our current understanding that ellipticals tend to be larger and more massive than spirals.

The results of this method for the first three Tasks in the GZ2 decision tree are shown in Figure 2.5. For each response in each Task, the average vote fraction is calculated as a function of redshift. Solid lines represent the weighted/non-debiased votes and the dotted lines are the debiased votes using this method (hereafter W13). The redshift dependence on vote fraction is very evident in the downward trend of the solid lines corresponding to responses which detect features, such as $f_{features}$ and f_{bar}

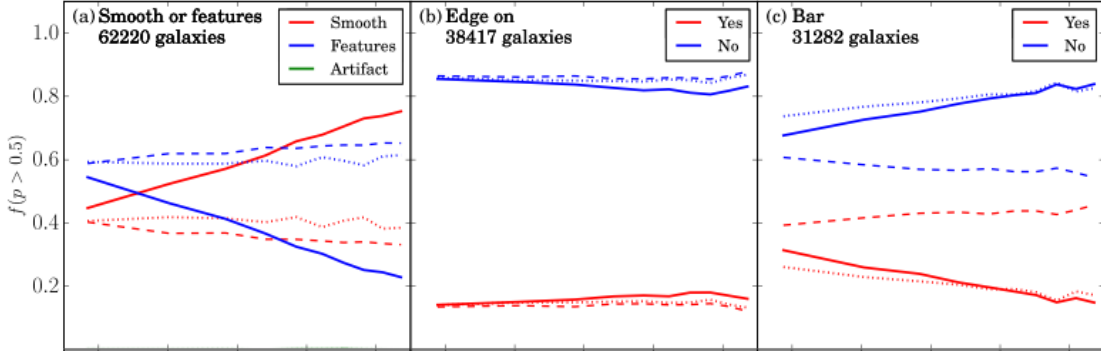


Figure 2.5 Placeholder - will make original later. Shows results of 2 debiasing methods for the first 3 tasks in GZ2

in this example. The dashed lines show the effect of the debiasing which attempts to flatten out the distribution. Full figures showing the results for all Tasks in the tree are available in Willett et al. (2013) (Figure 3) and Hart et al. (2016) (Figure 8). From 2013–2017, the debiased vote fractions calculated in this method were used in the majority of published Galaxy Zoo papers, and are used in the study described by Chapter 3.

Debiasing GZ2 and UKIDSS: H16 method

The W13 debiasing method is successful at adjusting the vote fractions to more accurately resemble the “true” distribution of morphologies at low redshift, but has two primary limitations. First, the rectangular binning of all three parameters (size, magnitude, and redshift) is only effective when the parent sample is large enough that sufficient data per bin remains available after the three dimensional binning. (For example, to require 10 bins in each parameter with at least 50 galaxies per bin, a parent sample must contain at minimum $N=10 \times 10 \times 10 \times 20 = 50,000$ galaxies, assuming a perfectly even distribution of values in each parameter). GZ2 is not so affected by this limitation, with a parent sample size of $\sim 250,000$ galaxies. However, this is only true when considering the debiasing of the first Task, which is asked of every galaxy. After this Task, the parent sample for computing a correction term decreases as not all Tasks are asked of every galaxy; for example, the Tier 4 Task which asks for the number of spiral arms is only seen by the majority of volunteers in 33,000 galaxies of the full GZ2 sample. Thus

debiasing this Task would require a smaller limit on the number of bins per dimension or the number of galaxies per bin, both of which decrease the robustness of the method. Even with a large parent sample for any Task, the rectangular binning is also limited by the inability to account for data which lie on the outer edges of the parameter space, as there tends to be insufficient data in the outer bins.

A new debiasing technique (hereafter H16) was developed by Galaxy Zoo member Ross Hart (Hart et al., 2016) which substitutes Voronoi binning for the rectangular method. Voronoi binning optimizes the shape and location of bins based on the desired signal for each bin; in this case, the number of galaxies per bin is set initially, and the bins are drawn to fulfill that requirement. In this way, the number of galaxies available for measuring the change in vote fractions for each bin is maximized. Thus, this method is more effective at debiasing smaller samples, where the three dimensional binning preserves the signal in each bin. This method was therefore used to debias the UKIDSS sample which is much smaller than GZ2, with only \sim 70,000 galaxies. An example of Voronoi binning the UKIDSS data in size and magnitude is shown in the left panel of Figure 2.6. Each size and magnitude bin is then Voronoi-binned by redshift.

The second limitation of the W13 method is that while it effectively corrects the vote fractions for any Task so that the average morphology is constant as a function of redshift, it does not account for the *distribution* of morphologies at low redshift. This produces good results when the corrected values are used for population studies, where the percentage of galaxies exhibiting a particular morphology are desired, but may not always reproduce accurate *individual* vote fractions. The R16 method instead corrects the high redshift vote fractions based on the change in distribution of vote fractions observed at low redshift, rather than comparing to only the average values. The first step of this method is shown in the right panel of Figure 2.6. For the low redshift bin of a given task, the cumulative distribution of vote fractions for each response is fit with a continuous function, which is used as the baseline distribution (similar to the baseline average votes in the W13 method.) The vote fractions making up the cumulative distributions at higher redshifts are then adjusted as needed to match the low redshift distribution as closely as possible.

Results of this method are shown and compared to W13 in Figure 2.5. The top row shows the average vote fractions as a function of redshift for the raw (solid lines),

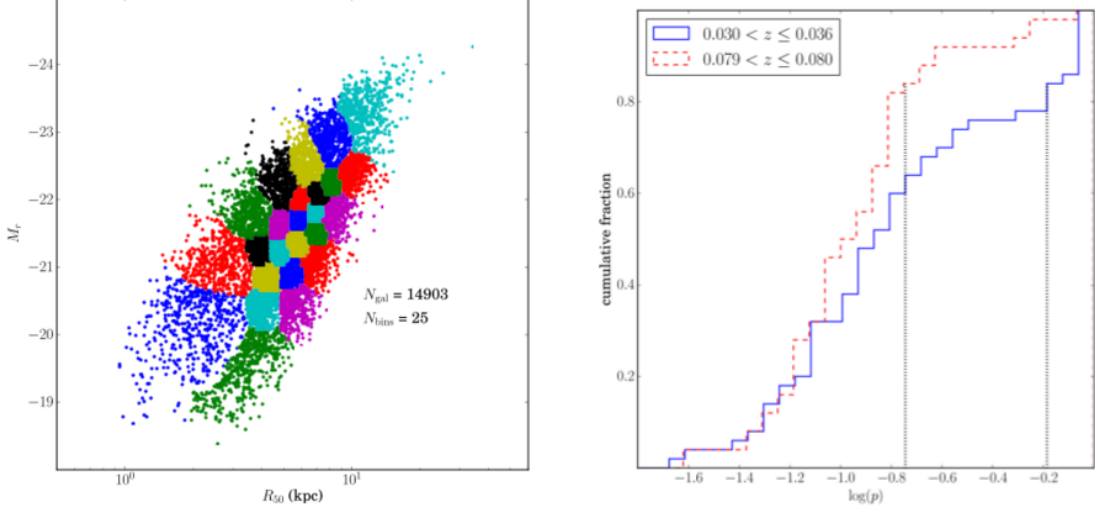


Figure 2.6 Placeholder - make my own later. Left shows how voronoi binning is done; compare to rectangular binning in W13. Right is cumulative distribution of some vote fraction at low and high redshift.

W13 debiased (dashed lines), and R15 debiased data (dotted lines). Both methods are succesful in stabalizing the average morphologies across redshift. The bottom row shows the distribution of vote fractions of a low-redshift bin and high redshift bin. It can be seen here that while both methods can reproduce the average vote fractions at low redshift, the R15 method is more succesful in reproducing the distribution of votes at low redshift.

Chapter 3

Bar AGN project

Basically Galloway et al. (2015)

Chapter 4

UKIDSS

4.1 Intro: wavelength dependence on morphology: optical and IR

Historically, visual morphological classification of galaxies has been conducted on optical images. Blue B-band images were the primary source dating back to Hubble’s classic tuning-fork classification scheme (Hubble, 1926) and in the subsequent modifications by Sandage (1961) and de Vaucouleurs (1963). The more recent and larger morphological catalogs also derive their classifications from rest-frame optical images, either single-band (de Vaucouleurs (1991) (B-band), Scarlata et al. (2007) (ACS I-F814W), Fukugita et al. (2007) and Nair & Abraham (2010) (SDSS g-band)) or color-composite (Lintott et al. (2008), Willett et al. (2013) (SDSS-gri)).

In the optical regime, the flux is dominated by young, hot stars; this results in an emphasis of spiral structure in the images, but they tend to have patchy appearances due to the abundance of star-formation regions in the arms. Optical images also are impacted by extinction due to dust, which can obscure features that tend to be composed of older stellar components (such as bars and bulges). Longer wavelengths are free of these effects, making them ideal for revealing the underlying “stellar backbone” of galaxies.

It is possible, then, to consider two morphologically distinct components of a galaxy: a gas-dominated Population I disk, and a star-dominated Population II disk. The Population I disk is most easily seen in the optical, revealing HII regions, cold HI gas,

and emission from young OB stars; these regions will tend to highlight flocculence in spiral structure. The Population II disk, on the other hand, traces the underlying mass distribution; consisting of the old, cooler stellar population, it is more easily seen at longer wavelengths. Block & Puerari (1999) even suggests that two separate classifications schemes should be required for all galaxies; one for the Population I disk, which can be probed in optical and ultraviolet images, and a Population II disk, for which longer wavelength images, free of dust extinction, would be required.

The extent to which the morphologies of the younger and older stellar populations are decoupled, however, is not yet clear. Early studies which directly compared optical and near-IR images found very significant differences between the two morphologies (Hackwell & Schweizer, 1983; Thronson et al., 1989; D. Block, 1991; Block et al., 1994). Block & Puerari (1999) goes as far as to suggest that there is no correlation between the two, and that the optically-defined Hubble tuning fork “does not constrain the morphology of the old stellar Population II disks.” However, all of the aforementioned studies only compared morphologies of either a single galaxy, or at most a handful, so these conclusions cannot be applied generally.

The advent of larger surveys incorporating near and mid-IR detectors enabled morphological comparisons between the two wavelength regimes on a much grander scale than had previously been achieved. New results contradicted those of the previous case-studies: in general, IR morphology was found to be well-correlated with optical morphology in larger samples of galaxies. Eskridge et al. (2002) compared near-IR H-band ($1.65\mu\text{m}$) Hubble-type classifications to B-band in a sample of 205 nearby spiral galaxies from the Ohio State University Bright Spiral Galaxy Survey (OSUBSGS). Applying deVaucouler’s classification system, they found an overall good correlation between the two morphologies, but on average galaxies from Sa through Scd appeared one T type earlier in the H band than in the B band. In the IR images the bulge tended to appear more prominent and the spiral arms less knotty, which resulted in the slightly earlier classifications. For the earliest (optically S0/a and Sa) and latest-type galaxies (optically Scd through Sm), no difference in morphologies was found. This is an expected result for the earlier-types, since these have little ongoing star formation and very little dust, so it is expected that both optical and IR morphologies are dominated by old stars. This result is less intuitive for the later-type galaxies, as these are

dominated by ongoing star formation. However, these galaxies are defined as having very weak or nonexistent bulges and poorly defined spiral structure. Since the main driver in the differences in morphology across wavebands was found in the intermediate spirals to be the relative prevalence of a bulge and difference in contrast and appearance of spiral arms, galaxies lacking these features should not, in fact, be expected to look different in the IR than the optical.

Buta et al. (2010) obtained similar results comparing optical and mid-IR ($3.6 \mu\text{m}$) images from the *Spitzer* Survey of Stellar Structure in Galaxies (S⁴G, Sheth et al. (2010)) in a large sample of 2,331 spiral galaxies. Like Eskridge et al. (2002), the optical and IR classifications were very well correlated, with the most significant differences occurring for S0/a to Sc galaxies, where the $3.6 \mu\text{m}$ were on average slightly earlier than the B-band classifications.

Infrared imaging is also often used in place of (or in addition to) optical to identify stellar bars (e.g. Mulchaey & Regan (1997); Knapen et al. (2000); Block et al. (2004); Sheth et al. (2008)). Like bulges, bars are primarily composed of old, red stars, and therefore better traced by longer wavelengths. In fact, it is not uncommon for an infrared bar to be completely invisible in the optical. Notable examples include NGC 1566 (Hackwell & Schweizer, 1983), NGC 1068 (Thronson et al., 1989; Scoville et al., 1988), NGC 309 (D. Block, 1991), NGC 4736 (Block et al., 1994), and NGC 4303 (Figure 1, Sheth et al. (2003)). This trend is not only limited to case-studies; for example, in a larger sample of 29 galaxies classified as unbarred in the optical, 50% of these were found to be barred in the near-IR images (Mulchaey & Regan, 1997).

The fraction of spiral galaxies which exhibit bars (defined as the bar fraction) has been measured extensively in optical images, and typically falls near 50% when bars of all strengths are considered (Masters et al., 2010)(should probably cite more). Since it is much more common to find an infrared bar in an optically unbarred galaxy than the reverse, it is expected that the bar fraction in the infrared will, in general, be higher than what has been measured in the optical. Some studies find a substantial increase: Seigar & James (1998) for example speculate that “bars may always be present in disks at some level”, based on finding a bar fraction of 90% when using infrared images (as compared to their optical measurement of 68%). Although their sample consisted of only 45 galaxies total, they claim this measurement should represent the general

population of spirals, because their selection was not biased towards barred galaxies. Other studies report similar increases in bar fraction in the infrared, albeit not quite as large. Knapen et al. (2000) in a similar sample size of 50 galaxies find a bar fraction in the infrared of 70%, a strong increase from the optical 50%. Eskridge et al. (2000) in sample of 186 galaxies measure a bar fraction of 72% in the infrared which is *double* that of their optical measurement. While these studies report significant increases in bar fraction as a function of wavelength, they do dispute the claim by Seigar & James (1998), emphasizing that at least 30% of galaxies in their sample are truly unbarred across all wavelengths.

Other more recent studies find larger bar fractions in the infrared, not significantly so. Whyte et al. (2002) measure an increase from 72% to 79% in a sample of 72 galaxies, while Sheth et al. (2008) reports 60% for both wavelengths. MenendezDelmestre et al. (2007) also found a slight increase from 63% to 67% in a sample of 151 galaxies, noting that although bars tended to appear stronger in the near-IR, on average they were not so weak in the optical as to become undetectable. Finally, Buta et al. (2010) also reported a similar result of 60% barred spirals, which was consistent with the fraction computed in optical RC3 classifications.

Now: segue into describing how we'll investigate these using a *much* larger sample than previously done, using GZ classifications. 2 goals: 1) investigate change in hubble-ish type in UKIDSS vs GZ2 (by looking at bulge question and arms-windyness), and 2) bar fraction, plus probably some case studies of galaxies whose morphologies change drastically.

4.2 UKIDSS sample

The UKIDSS sample is comprised of 71,052 infrared images of galaxies which had been previously optically classified in GZ2. The images were taken with the United Kingdom Infrared Telescope (UKIRT) as part of the UKIRT Infrared Deep Sky Survey (UKIDSS; Lawrence et al. (2007); Warren et al. (2007). The Large Area Survey (LAS) portion of UKIDSS covered the SDSS observations at high Galactic altitudes, allowing for full YZJHK coverage.

Morphological classifications for the UKIDSS sample were obtained via Galaxy Zoo,

UKIDSS		GZ2	
Filter	Depth (AB mag)	Filter	Depth (AB mag)
Y	21.13	g	22.2
J	20.91	r	22.2
K	20.25	i	21.3
seeing:	<1.2"	PSF width:	1.4" (median in r)
pixel scale:	0.4"	pixel scale:	0.396"

Table 4.1 Comparison of depth and resolution of the UKDISS and GZ2 images. The resolution between the two surveys is comparable, but the UKIDSS images are an average of ~ 1 magnitude shallower in all bands used to create the color-composite images that were classified.

where users were shown YJK color-composite images. The classification tree used was identical to that in GZ2, allowing a direct comparison of morphologies using the same vote fractions. Raw votes were counted and weighted by user consistency in the same manner as the GZ2 sample (details of this process are given in Chapter 2).

One major challenge in comparing the UKIDSS and GZ2 morphologies is to ensure that any differences measured are mostly driven by actual morphological differences between wavebands, and not due to varying instrumental parameters. Details of the instrumentation for both samples is shown in Table 4.1. The resolution of both sets are comparable - with similar pixel size and PSF widths, the ability to resolve finer features in the images should be consistent for both. The difference in depth, however, is significant: the SDSS gri bands used to create the color-composite images in GZ2 are on average ~ 1 magnitude deeper than what is achieved for the LAS YJK bands in UKIDSS. To minimize the impact the difference the difference in depth may have in comparing the two sets of images, the comparison sample is limited to the nearest and brightest galaxies. The sample is thus restricted to a volume-limit of $z < 0.06$ and $M_{r,\text{petro}} < -20.0$, which consists of 10,395 galaxies of the 54,238 with spectroscopic redshifts.

To further ensure that any observed difference in morphologies are due to physical (wavelength) dependencies, and not instrumentation, the sample is further restricted to only include galaxies for which the signal detected in the IR image extends to a

significant fraction of the galaxy’s total light profile. During preliminary visual inspection of side-by-side IR/optical images of the subjects, it was seen that for many of the optically-classified spirals, the arms in the IR images became so faint with respect to the bulge that there could be no fair comparison of morphologies using vote fractions. The two primary examples of this effect occurred firstly in GZ2-classified spiral galaxies which the majority voted as “smooth” in UKIDSS, due to the bulge being the only visible feature in the IR images (see top row in Figure 4.1 for an example of this effect.). Second, for optically-barred galaxies whose spiral arms were undetectable in the IR, only the bar remained visible, giving it the appearance and classification of an edge-on galaxy (bottom row in Figure 4.1). Not accounting for such cases could then give an underestimate of the total IR bar fraction.

4.2.1 S/N method for selecting equally-sized galaxies

To identify which galaxies are sufficiently detected in both the IR and optical images, the S/N profile of the IR J-band images is compared to the r-band petrosian radius. For disk galaxies whose surface brightness distribution follows an exponential profile, 99% of the galaxy’s total flux is enclosed by the Petrosian magnitude (Graham et al., 2005), which is defined as the flux measured within two Petrosian radii. Therefore, we can let $2 \times r_{\text{petro}}$ represent the radius that encloses the entire disk, which will be hereafter denoted as $r_{2\text{petro}}^r$. To properly compare morphologies of disk galaxies in IR and optical images, it must be ensured that a signal is detected in the J-band out to a significant fraction of that radius. This is done by computing the surface brightness profile in the J-band, and measuring the radius within which the S/N is greater than 3, which will be hereafter denoted as r_3^J . A cut is then placed on the volume-limited sample such that $r_3^J \geq 0.75r_{2\text{petro}}^r$, which retains $\sim 60\%$, or 6,484 galaxies considered suitable for a robust morphological comparison. The details of this process are described here.

The J-band cutouts were downloaded directly using the WFCAM Science Archive¹ . The signal to noise profiles are then computed on J-band sky-subtracted cutouts, where the sky subtraction is done using the PYTHON package PHOTUTILS BACKGROUND2D function. The noise is defined as the dispersion in the background flux, shown in the top-left panel of Figure 4.2. The background was fit to a Gaussian, and the noise was taken

¹ http://wsa.roe.ac.uk:8080/wsa/MultiGetImage_form.jsp

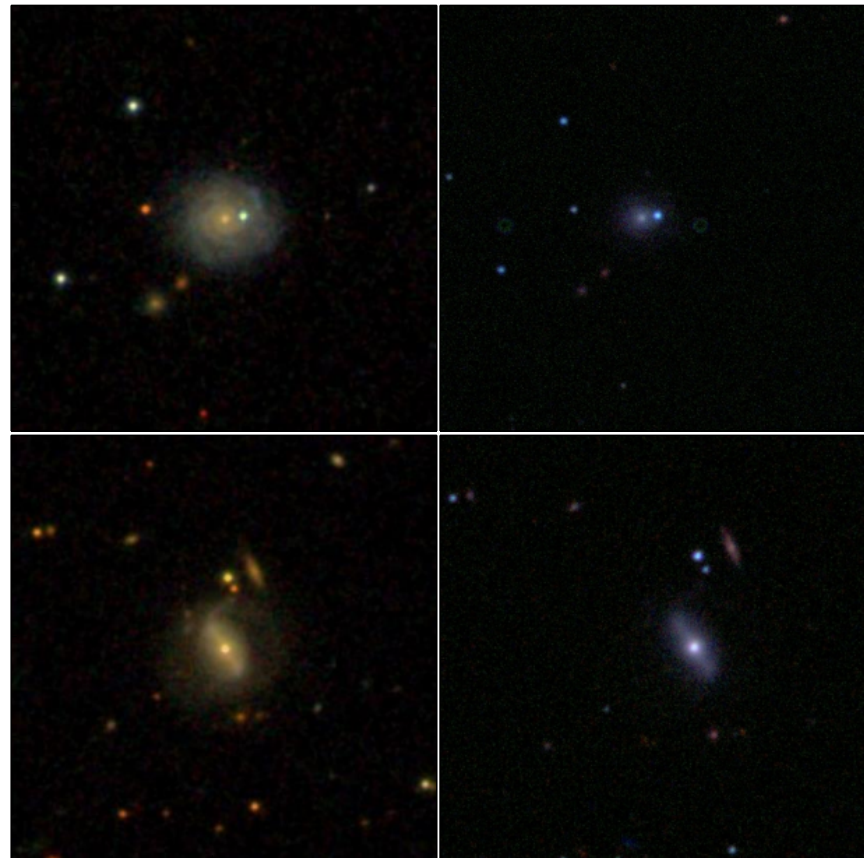


Figure 4.1 Examples of two galaxies whose morphological changes between optical and IR wavelengths was driven by a lack of light detectable in the IR relative to optical. **Top:** A galaxy classified as featured and spiral in the optical using GZ2 vote fractions, but smooth in the IR using UKIDSS vote fractions (dr7objid: 587726014553587781). **Bottom:** A galaxy classified as featured and barred in the optical using GZ2 vote fractions, but due to the complete disappearance of arms in the IR, only the bar is visible, giving it the appearance and classification of an edge-on galaxy (dr7objid: 587734305416871963)

as the resulting standard deviation value given by the fit. The signal was computed by calculating the average flux per pixel within circular apertures of varying radii from the center of the galaxy to the edge of the cutout. From these a signal-to-noise profile was generated for each galaxy; an example is shown in the top-right panel of Figure 4.2. The radius at which the S/N profile falls below $S/N=3$ (or in other words, the radius within which the S/N remains greater than 3, r_3^J), is recorded for each galaxy, represented as the green dashed line. The blue dashed line is drawn at $r_{2\text{petro}}^r$, representing the radius containing 99% of the flux, as described above. The ratio of r_3^J to $r_{2\text{petro}}^r$ is then used to evaluate whether the galaxy is sufficiently detectable in both wavelengths for a fair morphological comparison. The bottom row of Figure 4.2 shows the results of this method displayed on the color-composite images that are seen by GZ users. The circle on the optical image (left) shows $r_{2\text{petro}}^r$, and circle on the IR image (right) shows the J-band radius within which $(S/N)_J > 3$, r_3^J . In this example, $r_3^J = 0.62 \times r_{2\text{petro}}^r$, indicating that the radius at which the galaxy is detectable in the J band is only 62% that of what is visible in the r band. Given that the threshold for inclusion in the sample is $r_3^J/r_{2\text{petro}}^r \geq 0.75$, this galaxy is considered too faint in the IR with respect to the optical to fairly compare vote fractions.

Figure 4.3 shows the optical and IR images of galaxies, overlaid with circles of radii $r_{2\text{petro}}^r$ (optical, left) and r_3^J (IR, right), sorted by the ratio $r_3^J/r_{2\text{petro}}^r$. For small ratios (towards top of figure) it is obvious that the IR image is much too faint with respect to the optical image for a fair comparison of vote fractions, while for ratios closer to unity (towards bottom of figure), the images are much more comparable. The effect of $r_3^J/r_{2\text{petro}}^r$ on the difference in vote fractions is displayed in Figure 4.4. The left shows the distribution of the change in f_{features} vote fractions (explicitely: GZ2 f_{features} - UKIDSS f_{features}) for the optical and IR images as a function of $r_3^J/r_{2\text{petro}}^r$; the right shows the average change in f_{features} as a function of $r_3^J/r_{2\text{petro}}^r$. As expected, there is a much larger difference in vote fractions when the IR image does not show the full extent of the galaxy relative to the optical image (low $r_3^J/r_{2\text{petro}}^r$). This difference cannot be confidently attributed to a true morphological change, but rather a limitation on the instrumentation and therefore visibility of the galaxy. Therefore we limit the comparison to galaxies where $r_3^J/r_{2\text{petro}}^r \geq 0.75$ (dashed line in Figure 4.4, right), to increase confidence that a difference in vote fraction represents a physical morphological

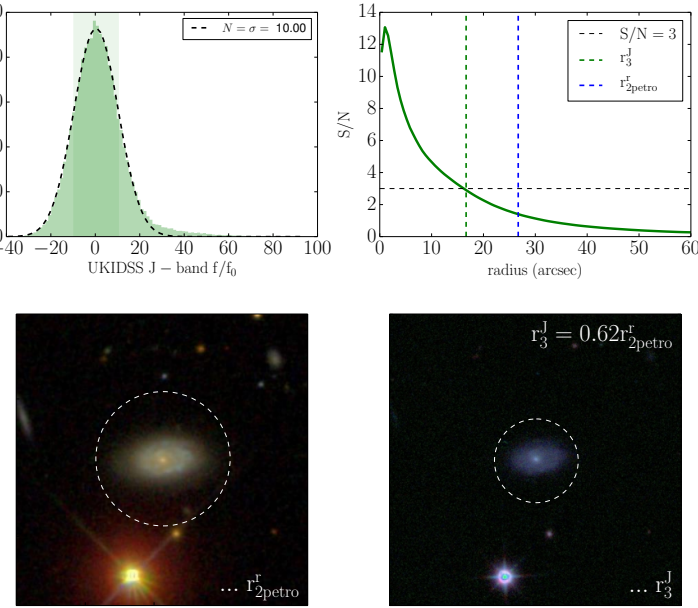


Figure 4.2 Example of the $r_3^J/r_{2\text{petro}}^r$ calculation of one galaxy (dr7objid=587722981747392587). **Top Left:** The sky-subtracted background of the J-band images are fit to a Gaussian to derive the noise N , which is given as the standard deviation of the fit. **Top right:** The signal to noise profiles of the J-band images. The radius at which the signal-to-noise falls below three is indicated by the green dashed line, and the threshold $S/N = 3$ is indicated by the horizontal black dashed line. The blue line shows twice the r-band petrosian radius $r_{2\text{petro}}^r$ for comparison. **Bottom:** Color-composite of the optical gri image (left) and IR YJK image (right). The dashed circles represent the radius $r_{2\text{petro}}^r$ (left) and r_3^J (right), derived as shown in the top row. The ratio of the two radii is given, showing that for this galaxy, the light in the IR image extends to 62% of the optical image.

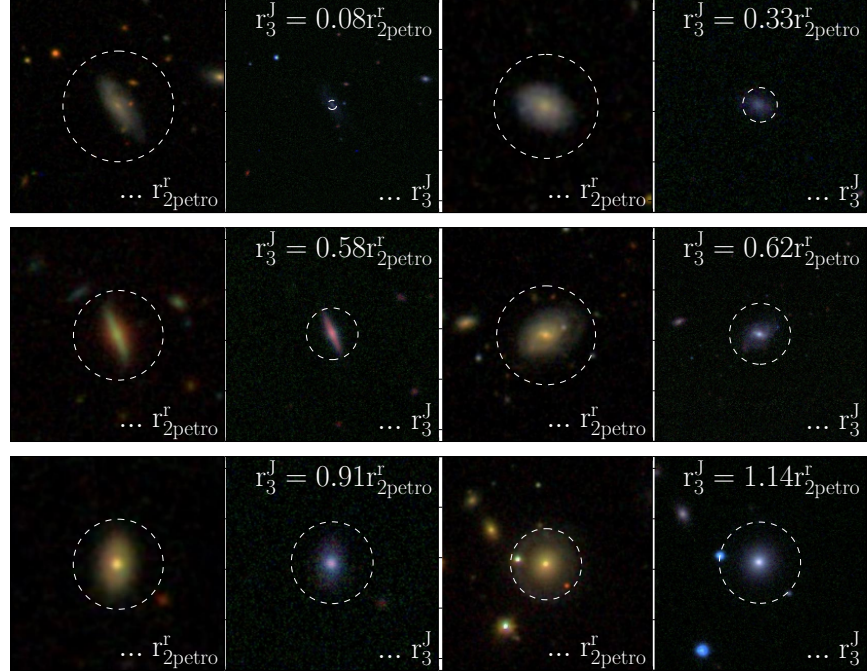


Figure 4.3 Example optical gri (left) and IR YJK (right) images of galaxies, sorted by $r_3^J/r_2^r_{\text{petro}}$. The circle on the optical image (left) shows $r_2^r_{\text{petro}}$, and circle on the IR image (right) shows the J-band radius within which $(S/N)_J > 3$, r_3^J .

difference between wavelengths.

4.3 Comparison of Hubble Types in Spirals

In this section the global morphologies seen in the infrared and optical are compared. As described above, the most recent studies found similar results when comparing the Hubble T-types of both wavelengths; in general, the morphologies are well-correlated, with the IR T-types being on average one T-type earlier than in the optical. The strongest difference occurred for the optically intermediate-type spirals. In the most

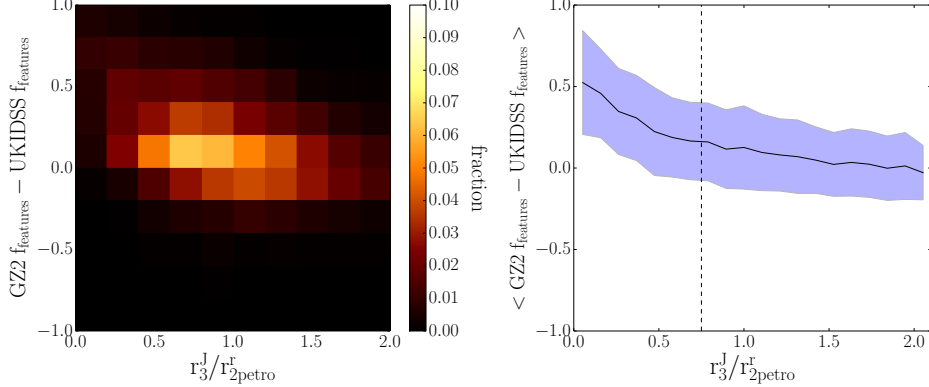


Figure 4.4 The change in GZ2 and UKIDSS vote fractions is strongest at low values of $r_3^J/r_2^r_{\text{petro}}$, where the light detectable in the J-band extends to a significantly smaller area than than the r-band images. **Left:** Distribution of the change in f_{features} from GZ2 to UKIDSS as a function of $r_3^J/r_2^r_{\text{petro}}$. **Right:** The average change in f_{features} from GZ2 to UKIDSS as a function of $r_3^J/r_2^r_{\text{petro}}$. The shaded region indicates the $1-\sigma$ dispersion around the mean. The dashed line at $r_3^J/r_2^r_{\text{petro}} = 0.75$ indicates the threshold below which galaxies are excluded from the comparison sample, due to the coverage of light in the J-band not reaching a significant area as represented in the r-band.

early type spirals (with very dominant bulge and very tight spiral arms), these features showed up equally well in the infrared. On the other extreme end, the very late type spirals (with almost no bulge and not well-defined arms) also showed no large change, since the relative size of the bulge and relative tightness of the arms were the main driver of the morphological differences between wavelengths. For the intermediate T-types, there was much more “wiggle room” for the bulges and arms to show more significant differences.

The first portion of this comparison will consider galaxies whose spiral arms are detected in both optical and infrared wavelengths.

As a proxy for Hubble types, the responses to the GZ Tasks related to tightness of the spiral arms and dominance of the bulge will be used, since these probe similar features to those that influence T-type classification. The Task related to arm tightness asks, “How tightly wound do the spiral arms appear?”, to which a user can choose one of three responses: “tight”, “medium”, or “loose”. For this analysis the fraction of users who answered “tight”, $f_{\text{tight arms}}$, will be used to assess the relative appearance of the

arms from optical to IR. The task related to bulge prominence asks, “How prominent is the central bulge, compared to the rest of the galaxy?” to which a user can respond “dominant,” “obvious,” “just noticeable,” or “no bulge.” For this analysis the sum of vote fractions for the first two responses $f_{\text{obv+dom}}$ will be used to measure the apparent size of the bulge relative to the galaxy.

Figure 4.5 shows the difference in vote fractions for arm tightness and bulge dominance between the GZ2 optical and UKIDSS infrared classifications, as a function of optical classification. The left plot shows that on average, spiral arms have a tighter appearance in optical wavelengths: $68.7\% \pm 4.0\%$ of spiral galaxies have lower $f_{\text{tight arms}}$ vote fractions in the IR images. For galaxies with optically very loose arms ($f_{\text{tight arms}} \sim 0$) or very tight arms ($f_{\text{tight arms}} \sim 1$), the infrared classifications tend to agree. For intermediately tight optical spiral arms ($0.2 < f_{\text{tight arms}} < 0.8$), the UKIDSS vote fraction tends to be lower than the optical by ~ 0.3 on average. This supports the work by Eskridge et al. (2002) and Buta et al. (2010) who find slightly earlier IR classifications in intermediate-type spirals. The right panel shows the change in bulge prominence as a function of optical bulge prominence. Here the effect is even stronger: the fraction $f_{\text{obv+dom}}$ is larger for the IR images in $95.8\% \pm 1.8\%$ of the galaxies, indicating the bulge is almost always more prominent in IR images than optical images. This again is in perfect agreement with studies, ie Eskridge et al. (2002), who conclude that the main drivers of the change in T-type in spirals are “the relative prevalence of the bulge and the difference in contrast and appearance of spiral arms”. Here we see the same effect, and can add to the discussion that the appearance of the bulge is a stronger driver of the observed change in T-type than the spiral arm contrast. These results differ slightly than Eskridge et al. (2002) in the case of galaxies with significantly small or no bulges; in their sample, if a bulge is not detectable in one band, it generally will not be detected in the other: “Galaxies with no bulge... will not look substantially different in the near-IR than in the optical, and will thus be classified essentially the same on average.” However our sample finds a small population of galaxies where this is not the case, as seen in the left-most columns of the right plot in Figure 4.5. Here little to no bulge is seen in the optical images (signified by a vote fraction $f_{\text{obv+dom}} \leq 0.2$), while the IR images of the same galaxies have vote fractions up to $f_{\text{obv+dom}} \sim 1$.

So far the appearance of spiral arms visible in both the optical and infrared have been

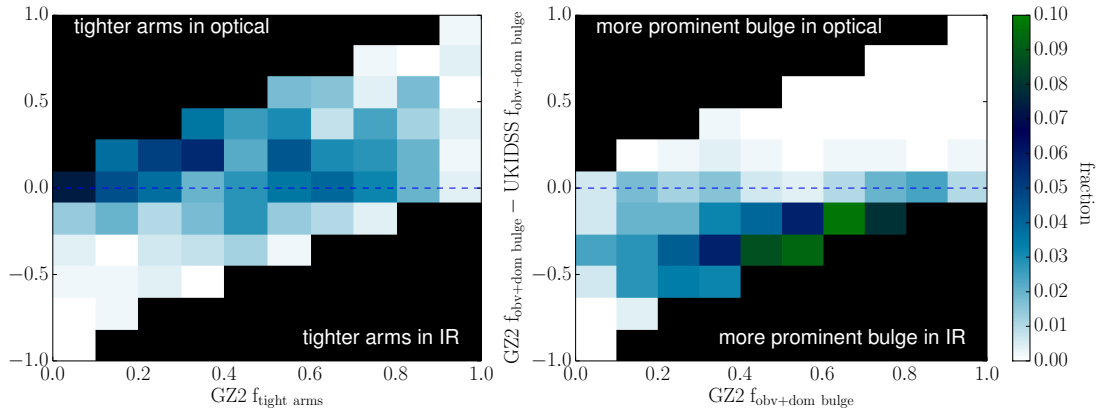


Figure 4.5 IR images of galaxies tend to have a looser appearance of arms and more prominent bulges than in optical images. Shown is the difference between optical and IR $f_{\text{tight arms}}$ as a function of optical/GZ2 $f_{\text{tight arms}}$ (**left**), and difference between optical and IR $f_{\text{obv+dom}}$ as a function of optical/GZ2 $f_{\text{obv+dom}}$ (**right**) for 502 galaxies which were classified as spiral in both IR and optical images. The colors represent the fraction of galaxies that populate any given bin, and bins which could not represent a possible difference in vote fraction ($\Delta f > f$ or $\Delta f < f - 1$) are colored black. The blue dotted line in both represents a difference in vote fraction of 0, such that galaxies above the line have larger IR vote fractions for the feature represented in each plot, respectively.

compared; on average, GZ infrared morphologies are slightly earlier than the optical, a result of a looser appearance of the arms and more prominent bulges. But what of the optically spiral galaxies whose arms disappear in the IR? Of the 1,042 optical spirals in the volume and S/N limited sample, 540 (52%) of these were not classified as spirals in the IR. These types will be hereafter referred to as SONIs (Spiral in Optical but Not Infrared) for convenience. The most common morphological classes of galaxies which do not exhibit spiral arms are ellipticals, S0s, and edge-on disks (which may or may not truly have spiral arms, but cannot be discerned due to orientation angle). This section will explore which of these classes SONIs tend to occupy in the IR.

Figure 4.6 shows the different pathways galaxies in the UKIDSS sample follow through the decision tree. The left flow diagram shows the breakdown of morphologies of all galaxies in the volume-limited sample, while the right diagram includes only the SONIs. Galaxies which follow the spiral pathway must first be classified as featured (T00), then not edge-on (T01). At this point the not edge-on featured galaxies can follow the 'spiral' or 'not spiral' path (T03). Those marked as spirals are classified by how tight the arms appear (T09) and how many arms are present (T10). Last, both the spirals and not-spirals are classified by bulge prominence (T04). As a result of this type of decision tree, there are several pathways galaxies may take to ultimately obtain a "not spiral" classification. They may be classified from the beginning as not featured (as ellipticals or star/artifacts), or they may be featured but edge-on, or they may be featured and not edge-on, and still show no spiral arms.

The diagram on the right shows which of these paths SONIs tend to take, resulting in their ultimate classification of "not spiral" in the IR. 72% of SONIs follow the elliptical path; that is, the optically-visible spiral arms must become so faint that all that can be seen is the central bulge, which by eye becomes discernable from a full spheroidal galaxy. 28% are classified as both featured and not edge-on. One might hypothesize a majority of these exhibit stellar bars, which drives the "featured" classifications when there are no spiral arms to do so. However, there is no excess of strong bars detected; only 24% of the not edge-on featured SONIs are strongly barred, which is actually lower than that of the full sample (33%). Since the diagram flows are determined by a plurality of votes for each Task, however, the possibility of weak bars of driving the "featured" classification is not accounted for here. Therefore most of the galaxies on this path

are likely either weakly barred, and/or retain evidence of both an underlying disk and a bulge, with enough contrast to keep them from being classified as purely elliptical. However it is clear that the bulge is very close to dominating the total light distribution in many of these galaxies; for SONIs, 90% are classified as having an either obvious or dominant bulge, as compared to 83% showing obvious or dominant bulges in the full sample.

4.4 Bar Fraction

This section will focus on the properties of bars observed in the two wavelengths: first by measuring the fraction of bars detected, and secondly the relative strengths. To avoid possible confusion in this portion of the text, two similar quantities are defined explicitly here: the *bar fraction* is defined as the ratio of barred galaxies to total galaxies in a sample, and f_{bar} is the *bar vote fraction*, which is the fraction of users who detected a bar in an image of an *individual galaxy*.

To measure the fraction of barred galaxies, the sample is first limited to galaxies for which there were at least 20 answers to the question in the decision tree that asks, “Is there a sign of a bar feature through the center of the galaxy?” This cut serves two purposes: first, it provides good statistics in computing f_{bar} for each galaxy (see Figure stats). Second, for the UKIDSS sample which has at maximum 40 total classifications per galaxy, this places an indirect cut on the preceding vote fractions $f_{\text{features}} \geq 0.5$ and $f_{\text{not edge on}} \geq 0.5$. This intrinsically limits the sample to featured, not edge-on galaxies, which is precisely the sample desired for computing the bar fraction, as bars are nonexistent in elliptical galaxies, or indetectable in highly-inclined edge-on galaxies. For the GZ2 sample, however, a significant portion of the galaxies have between 40-60 total classifications; so, a cut of $N_{\text{bar}} \geq 20$ would not guarantee the same minima for the preceding vote fractions. Therefore direct cuts of $f_{\text{features}} \geq 0.5$ and $f_{\text{not edge on}}$ are additionally placed on the GZ2 classifications to ensure the same sample selection for both wavelengths.

Figure 4.11 compares f_{bar} measured in the UKIDSS and GZ2 images for galaxies which were classified as featured and not edge-on in both samples. In this study, any galaxy for which $f_{\text{bar}} \geq 0.3$ is classified as barred. The dashed lines in the figure mark

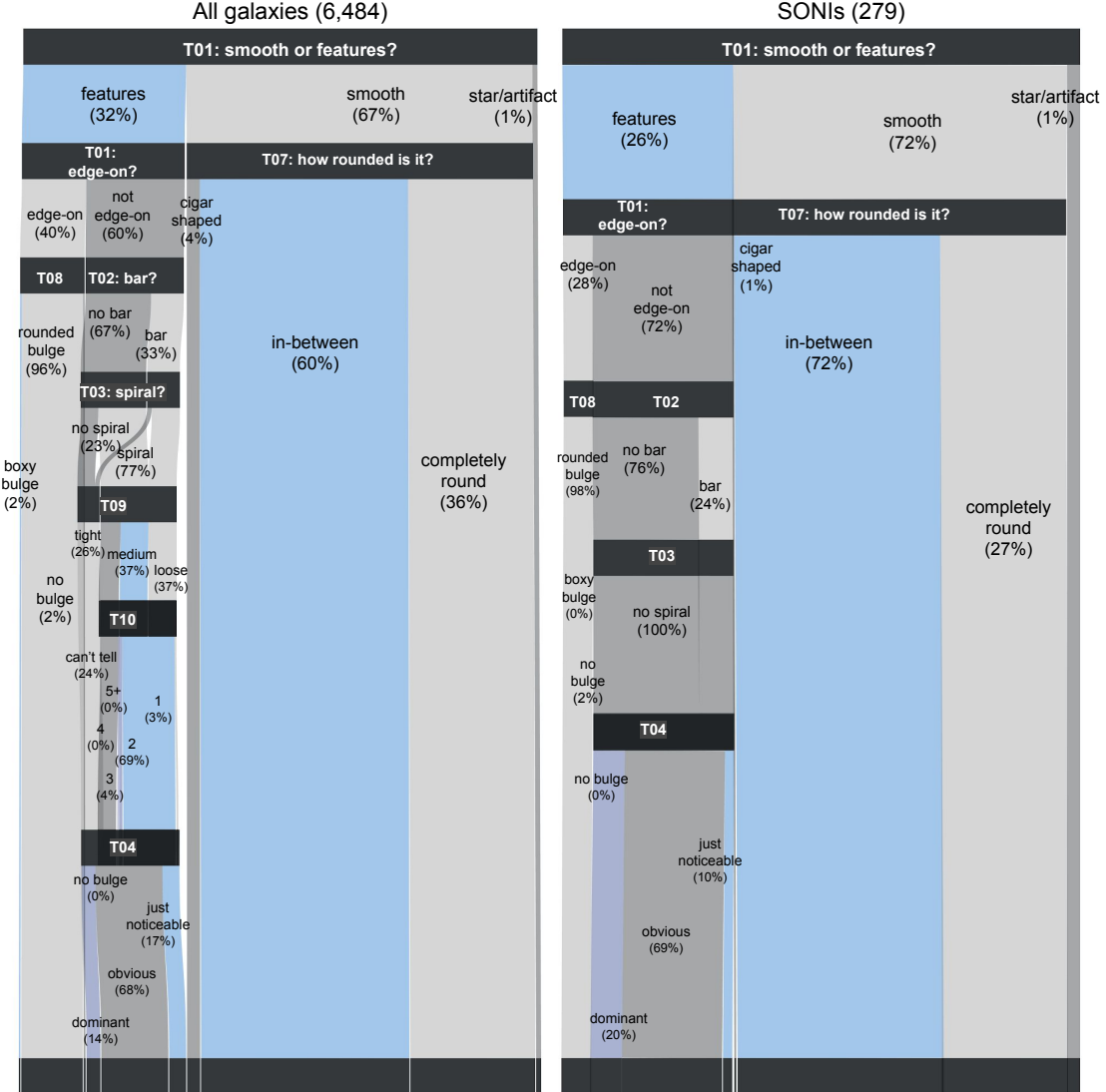


Figure 4.6 Flow diagram showing the breakdown of morphologies in the UKIDSS sample. **Left:** 15,491 galaxies in the volume-limited sample. **Right:** 2,346 SONIs: galaxies which were classified as spiral in the optical GZ2 classifications but do not follow the spiral path in the UKIDSS classifications.

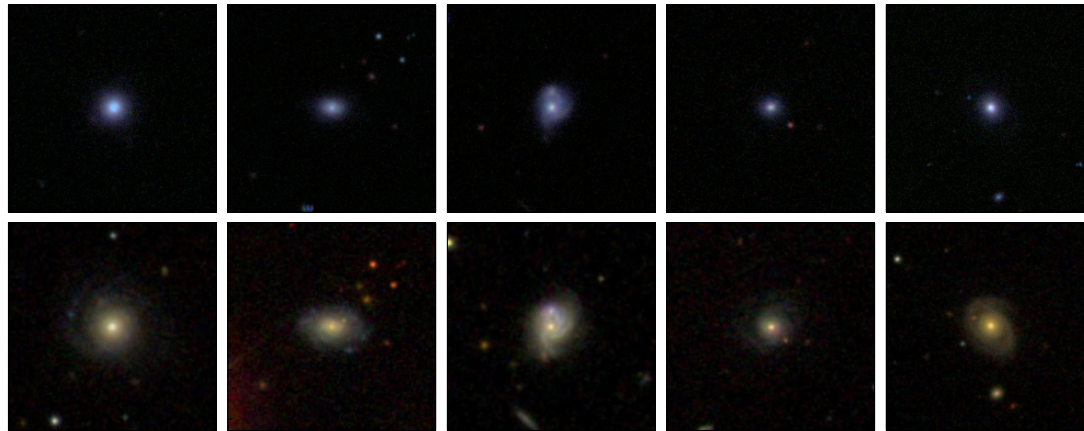


Figure 4.7 Example images of galaxies which were classified as spiral in optical GZ2 classifications but followed the “smooth” path in the UKIDSS classifications.

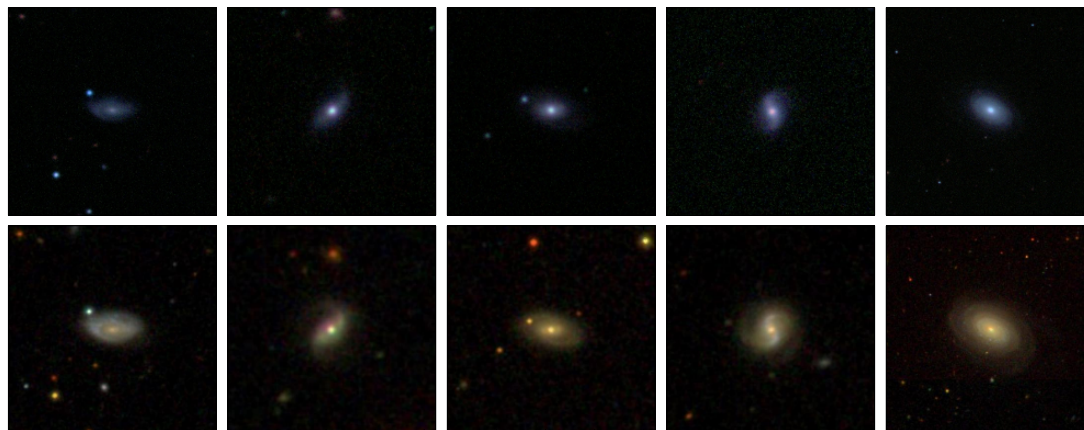


Figure 4.8 Example images of galaxies which were classified as spiral in optical GZ2 classifications but followed the “featured, not edge-on, no spiral” path in the UKIDSS classifications.



Figure 4.9 Example images of galaxies which were classified as spiral in optical GZ2 classifications but followed the “featured, edge-on” path in the UKIDSS classifications.

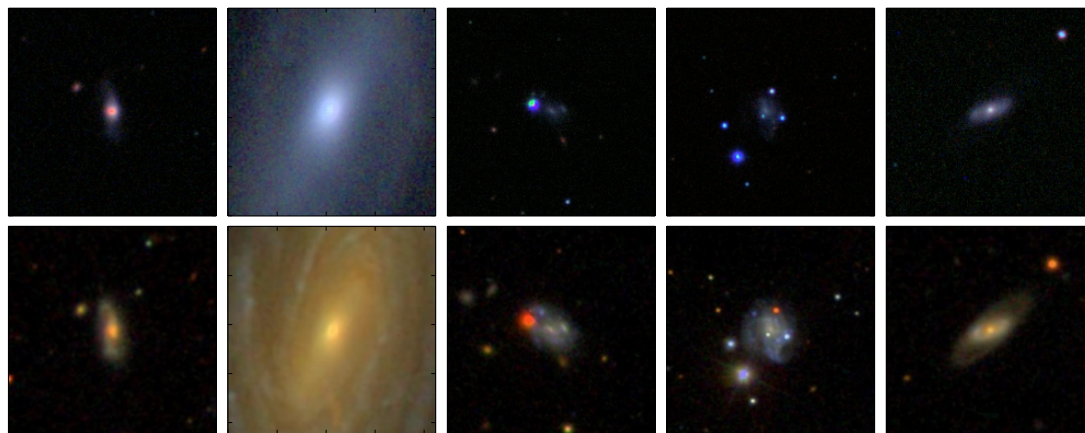


Figure 4.10 Example images of galaxies which were classified as spiral in optical GZ2 classifications but were classified as star/artifact in the UKIDSS classifications.

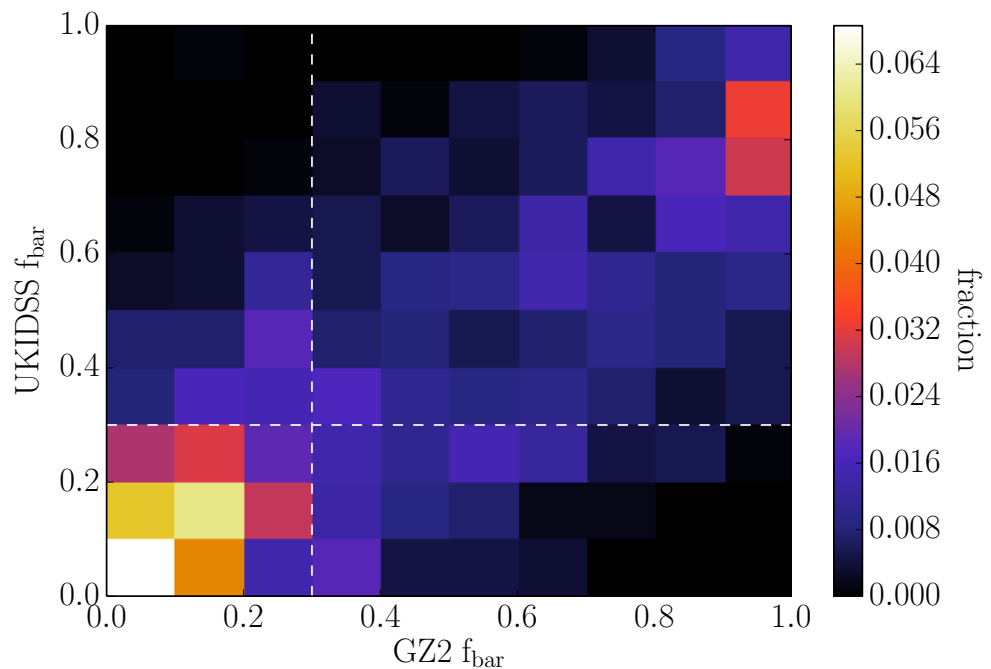


Figure 4.11 Dotted lines indicate the threshold for bar classification; $f_{bar} > 0.3$. Galaxies shown had at least 20 people answering the bar question.

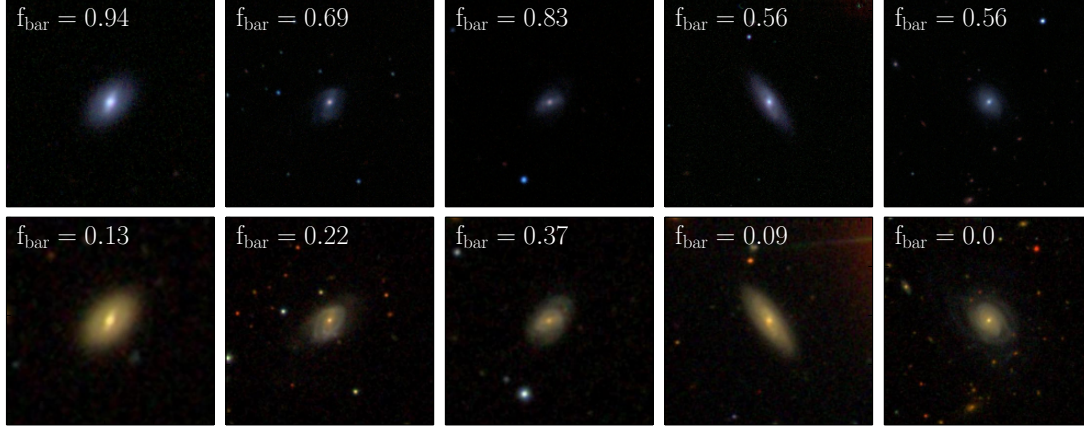


Figure 4.12 Galaxies classified as barred in optical GZ2 and unbarred in infrared UKIDSS.

this threshold, such that galaxies to the right of the vertical dashed line were classified as barred in the optical images, and those above the horizontal dashed line were classified as barred in the IR images. Four regions can be defined in this way: The top right region of the plot represents galaxies classified as barred in both wavelengths, the bottom right shows those which are unbarred in both, the top left shows those which are barred in the IR but not the optical, and the bottom left shows those which are barred in the optical but not IR.

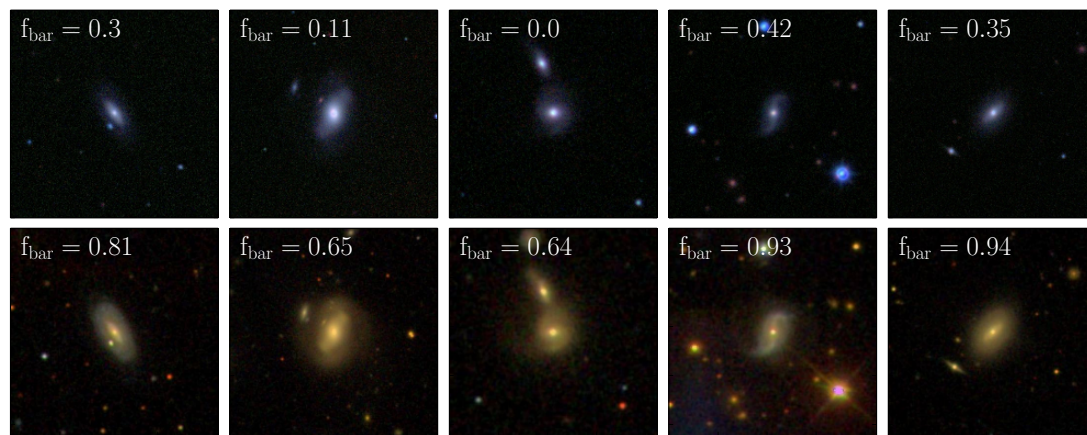


Figure 4.13 Galaxies classified as barred in infrared UKIDSS and unbarred in optical GZ2.

Chapter 5

Using FERENGI to correct f_{features} for redshift-induced classification bias

5.1 Intro

The GZ vote fraction f_{features} plays a crucial role in the majority of science cases that use Galaxy Zoo classifications. It represents the fraction of users who answered “feature or disk” to the first question in the decision tree, and is used to distinguish elliptical/spheroidal galaxies from those with features. Many studies aim to measure the population of galaxies exhibiting certain features such as bars (examples), spiral arms (examples), [dump stuff in this list]. In each of these, f_{features} is necessary for creating the sample of galaxies which could potentially contain the feature in question. This is typically achieved by setting a cut, such that all galaxies with f_{features} greater than that threshold are considered to be candidates for that study.

While f_{features} is not a true probability, the measurement is intended to be consistent among all galaxies; that is, two galaxies with similar f_{features} values should have similar likelihoods of being featured (or not featured). This has been shown to be true at low redshift by comparing the f_{features} values to expert classifications (reference Willet et al. 2013); there is a strong correlation between this vote fraction and whether the galaxy

was expertly classified as a disk or an elliptical [expand on what W13 actually did].

For distant galaxies, however, we observe that f_{features} is not consistent with nearby galaxies. As galaxies are observed at higher redshift, the images are inherently less resolved, and smaller features are more difficult to identify. This causes a decrease in f_{features} than what would be expected if the galaxy had been observed at $z = 0$. Figure [make a figure] shows this effect: [describe some figure, probably a bunch of galaxies that are obviously spirals but with very diff. f_{features} values at diff. redshifts.] Therefore, two identical galaxies, imaged at different redshift, may have small to drastic differences in their f_{features} measurement. In order to keep f_{features} a value correlated with the likelihood of having features that is consistent for *all* galaxies, this bias must be corrected.

A method for correcting redshift bias in the GZ vote fractions was developed and implemented in prior Galaxy Zoo projects (cite GZ1 and GZ2), which contained nearby ($z < 0.2$) galaxies imaged by the SDSS. A correction factor to the classification fractions measured at the higher redshifts was applied by matching the mean vote fractions of those at the lowest redshift. This technique was valid under the assumption that, within this redshift range, there would be no cosmological evolution of galaxies, and therefore any change in the mean vote fraction for any morphology with redshift was purely due to this observational bias, and not due to a genuine difference in morphological populations.

In GZH, the redshift range is large enough that cosmological evolution of the morphologies of galaxies is expected, and therefore the previous method of correcting redshift-bias will not work. Instead, we have developed a new method of measuring the change in f_{features} as a function of redshift using a set of simulated FERENGI images of galaxies, described in the next section. These images have been classified by volunteers in Galaxy Zoo in the same way as the GZH sample. This chapter will describe how we measure a correction factor for f_{features} using these data as a function of redshift at fixed surface brightness, and apply the correction to the GZH sample.

5.1.1 The FERENGI code

The Full and Efficient Redshifting of Ensembles of Nearby Galaxy Images code (FERENGI, Barden et al. (2008)) is an IDL procedure that generates simulated images of

nearby galaxies viewed at higher redshifts, taking into account cosmological effects such as surface brightness dimming and bandpass shifting. Artificially redshifted samples of galaxies, for which the intrinsic morphologies are already known from low-redshift observations, are useful for studying the impact these effects have on observed galaxy morphologies. For Galaxy Zoo, such images are particularly useful for measuring the effects of redshift on the volunteer classifications. Through classifications made on a set of artificially redshifted galaxies, any dependence they might have as a function of redshift can be measured, allowing a correction to be applied to classifications on images of real, high-redshift galaxies. The details of this type of debiasing technique will be described in Section 5.3. This section will first provide a brief summary of how the FERENGI code performs the artificial redshifting.

To create realistic images that mimic the seeing and resolution of HST ACS, the FERENGI redshifting procedure consists of four steps (explained in detail in Barden et al. (2008), but here a simplified outline):

i: Modify angular size and surface brightness

FERENGI first rescales the input image by computing the angular size transformation of the galaxy from its input redshift z_i to output redshift z_o . The angular size a of a distant object is proportional to $a \propto d/(1+z)^2$ (using $\tan(a)=a$ for small angles), where d is the luminosity distance to the object. In units of pixels, the transformation from input angular size n_i to output n_o can be expressed as:

$$\frac{n_o}{n_i} = \frac{d_i/(1+z_i)^2}{d_o/(1+z_o)^2} \frac{p_i}{p_o} \quad (5.1)$$

with an input pixel scale p_i (in this thesis $p_i = 0.396''/\text{pix}$ corresponding to SDSS) and p_o ($0.03''/\text{pix}$, corresponding to ACS). From here a transformation between the observed fluxes is computed, assuming the absolute magnitude is conserved at both redshifts.

FERENGI also offers an option to apply an evolutionary correction to the absolute magnitude, which is helpful for a fair comparison of real and artificial high redshift morphologies. Artificially redshifted galaxies will appear much dimmer than their low redshift counterparts if absolute magnitude is conserved. Since galaxies intrinsically tend to be brighter at high redshift, visual classification of real galaxies cannot be compared as accurately to dimmer, simulated galaxies. To brighten galaxies in a similar

way to real galaxies, a magnitude correction e can be input using a linear function:

$$M_{evo} = e \times z + M \quad (5.2)$$

where e represents the magnitude difference between two redshifts separated by $\Delta z = 1$.

ii: Account for bandpass shifting

As a consequence of cosmological expansion, the flux from a source measured using a broadband filter will not, in general, perfectly correspond to the rest-frame flux emitted at the target wavelength range of the filter. Rather, since observed wavelengths are redder than emitted wavelengths as a function of redshift ($\lambda_{obs} = \lambda_{rest-frame}(1+z)$), filters will tend to pick up light that is bluer (in the galaxy's rest-frame) than its target wavelength; this effect is known as *bandpass shifting*. In order to produce fluxes that mimic those measured by ACS at high redshifts, FERENGI simulates the bandpass shifting effects by applying a correction to the output flux calculated via the IDL routine KCORRECT, which incorporates spectral template models from Bruzual & Charlot (2003), to measure the expected shifts in flux for a given output filter.

iii: Point Spread Function and noise

In order to best mimic the HST ACS resolution, the image is then convolved with a PSF created to be as close as possible in shape and width to the ACS PSF. This is done by deconvolving a typical ACS PSF with the input SDSS PSF for each galaxy. This technique works well in general but has limitations - mainly, the widths of the in- and output PSFs must be sufficiently different. If they are comparable, the convolving function can become too narrow. In these cases, the image will be introduced to noise which results in ringing patterns and other oddities (examples of images with this effect are shown in Section 5.4.1). Since the difference in PSF widths increases with redshift, this imposes a minimum redshift at which FERENGI can successfully create images for any given galaxy (discussed more in Section 5.2). Last, Poissonian noise is added to each pixel.

5.2 The FERENGI sample

To generate an artificially redshifted sample of galaxies to be used in debiasing the Galaxy Zoo: Hubble catalog, a source sample was generated¹ consisting of 288 galaxies from SDSS, all of which were previously classified in GZ2. These galaxies were chosen to span a wide range of morphologies, surface brightnesses, and redshifts. Seven morphological classes were considered: spiral galaxies, edge-on disks without a bulge, edge-on disks with a bulge, face-on disks with a bulge, galaxies with any features, galaxies undergoing mergers, and barred galaxies. For each of these categories, galaxies were chosen with from three “strength” bins, defined using the GZ2 vote fractions. Weak strengths were defined as having $f_{class} < 0.2$, intermediate as $0.2 < f_{class} < 0.8$, and strong as $f_{class} > 0.8$. In each strength bin, galaxies were also chosen to represent three different surface brightnesses: $\mu_r > 21.5$, $20.5 < \mu_r < 21.5$, and $\mu_r < 20.5$. Finally, from each morphological class, strength, and surface brightness bin, one galaxy was chosen for four redshift bins: $z < 0.013$, $0.013 < z < 0.02$, $0.02 < z < 0.025$, and $z > 0.025$, with the exception of the bar class, in which two galaxies were chosen for each redshift bin, doubling the sample size for that class.

The 288 SDSS galaxies were processed with the FERENGI code to mimic *HST* imaging parameters², in order to ultimately measure and correct any redshift-dependant biases in the classifications of the real *HST* images. I-814 and V-606 images, chosen to match the *HST* ACS AEGIS imaging, were output for each subject at a range of redshifts and with a range of applied evolution factors. The range of simulated redshifts possible for any galaxy is dependent on the intrinsic redshift and size of the source galaxy, since the simulated images cannot be resampled at better angular resolution than the original SDSS data. This imposes a minimum simulated “target” redshift that can be achieved for each galaxy. For the lowest redshift bin in the source sample ($z < 0.013$), galaxies could be redshifted the full range of $0.3 < z < 1.0$, in increments of $dz = 0.1$. For the second lowest redshift bin, galaxies could only be redshifted in the range $0.5 < z < 1.0$, for the third, galaxies could be redshifted in the range $0.8 < z < 1.0$, and for the highest redshift bin, galaxies were only redshifted in FERENGI to $z = 1.0$. Only galaxies which were redshifted the full range were considered in the

¹ The source sample for FERENGI was created by the Galaxy Zoo science team in 2012.

² This work was done by Edmond Cheung, a Galaxy Zoo science team member.

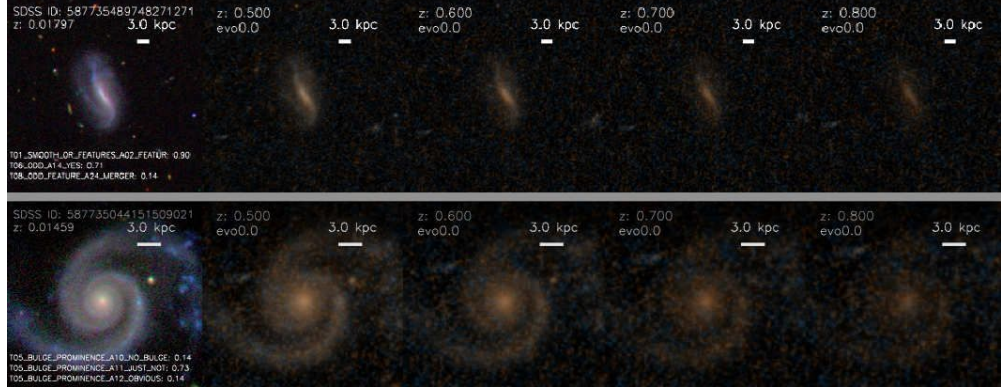


Figure 5.1 Examples of two SDSS galaxies which have been run through the FERENGI code to produce simulated *HST* images. The measured value of f_{features} from GZH for the images in each panel are (1) Top row: $f_{\text{features}} = (0.900, 0.625, 0.350, 0.350, 0.225)$ and (2) Bottom row: $f_{\text{features}} = (1.000, 0.875, 0.875, 0.625, 0.375)$.

debiasing procedure outlined in the next section (5.3.1), because the method calibrates galaxies to a low redshift of $z = 0.3$, data for which is not available for galaxies in the remaining three redshift bins. Last, for each simulated redshift, a range of evolution factors was applied from $0 < e < 3$ in increments of $de = 0.5$.

The final FERENGI sample totals 6,624 simulated images which were classified as part of GZ4, using the same decision tree as used in GZH. The debiasing technique described next (Section 5.3) used only the 4,446 images corresponding to the 72 galaxies which were redshifted the full $0.3 < z < 1.0$ range. Because the debiasing method takes into account surface brightness as a parameter, photometry was measured for all images using SExtractor³. The mean surface brightness μ within effective radius (R_e) was calculated as:

$$\mu = m + 2.5 * \log_{10} (2 \times (b/a) \times \pi R_e^2) \quad (5.3)$$

where m is MAG_AUTO in the I_{814W} band, (b/a) is the galaxy ellipticity (the profile RMS along the semi-major and -minor axes), and R_e is the 50% FLUX_RADIUS converted into arcsec.

³ SExtractor measurements for the original FERENGI sample were done by Tom Melvin, a former Galaxy Zoo science team member.

5.3 Measuring the drop in f_{features} as a function of z and μ using FERENGI data

5.3.1 Identifying “correctable” and “lower limit” samples.

The objective is to use the simulated data from FERENGI to predict, for a galaxy imaged at a redshift z , and with a measured $f_{\text{features},z}$ value, what its f_{features} value *would have been* if it had been viewed at $z = 0.3$. This predicted value is defined as the “debiased” vote fraction $f_{\text{features,debiased}}$, and is calculated by applying a correction to the measured value of f_{features} .

The amount that a galaxy’s f_{features} vote fraction must be corrected is assumed to primarily depend on the apparent size and brightness of the galaxy. As described in 5.1, these factors will affect the overall clarity of the image viewed by the GZ volunteers, which in turn affects the likelihood of being able to identify distinct feature. The apparent size and brightness are controlled by both intrinsic parameters (absolute size and luminosity), and extrinsic (distance to the galaxy). The change in f_{features} then is measured as a function of redshift (z , an extrinsic feature, measuring distance to the galaxy), and surface brightness (μ , an intrinsic feature, taking into account both brightness and size).

Figure 5.2 shows the change in f_{features} for FERENGI galaxies in bins of redshift and surface brightness. Points in each z, μ represent individual FERENGI galaxies. On the x-axis of each bin is the value of f_{features} measured in that galaxy’s $z = 0.3$ image (the lowest redshift of the simulated images). On the y-axis of each bin is the value of f_{features} measured in that galaxy’s $z = z$ image, where z corresponds to the redshift associated with that bin. As predicted, the value of f_{features} measured at a higher redshift, z , is, in general, *lower* than the value measured at lower redshift, $z = 0.3$, *for the same galaxy*. This effect is strongest as redshift increases (to the right in Figure 5.2) and as surface brightness decreases (upwards in Figure 5.2).

A reliable predicted value can be obtained so long as the relationship between $f_{\text{features},z}$ and $f_{\text{features},z=0.3}$ is single-valued; that is, for a given $f_{\text{features},z}$, there is exactly one corresponding value of f_{features} at $z = 0.3$. Unfortunately, this is *not* always the case. Figure 5.3 shows f_{features} measured at $z = 1$ vs f_{features} measured at $z = 0.3$ for FERENGI galaxies with average surface brightnesses $\langle \mu \rangle \geq 20.8$ (a zoomed-in version

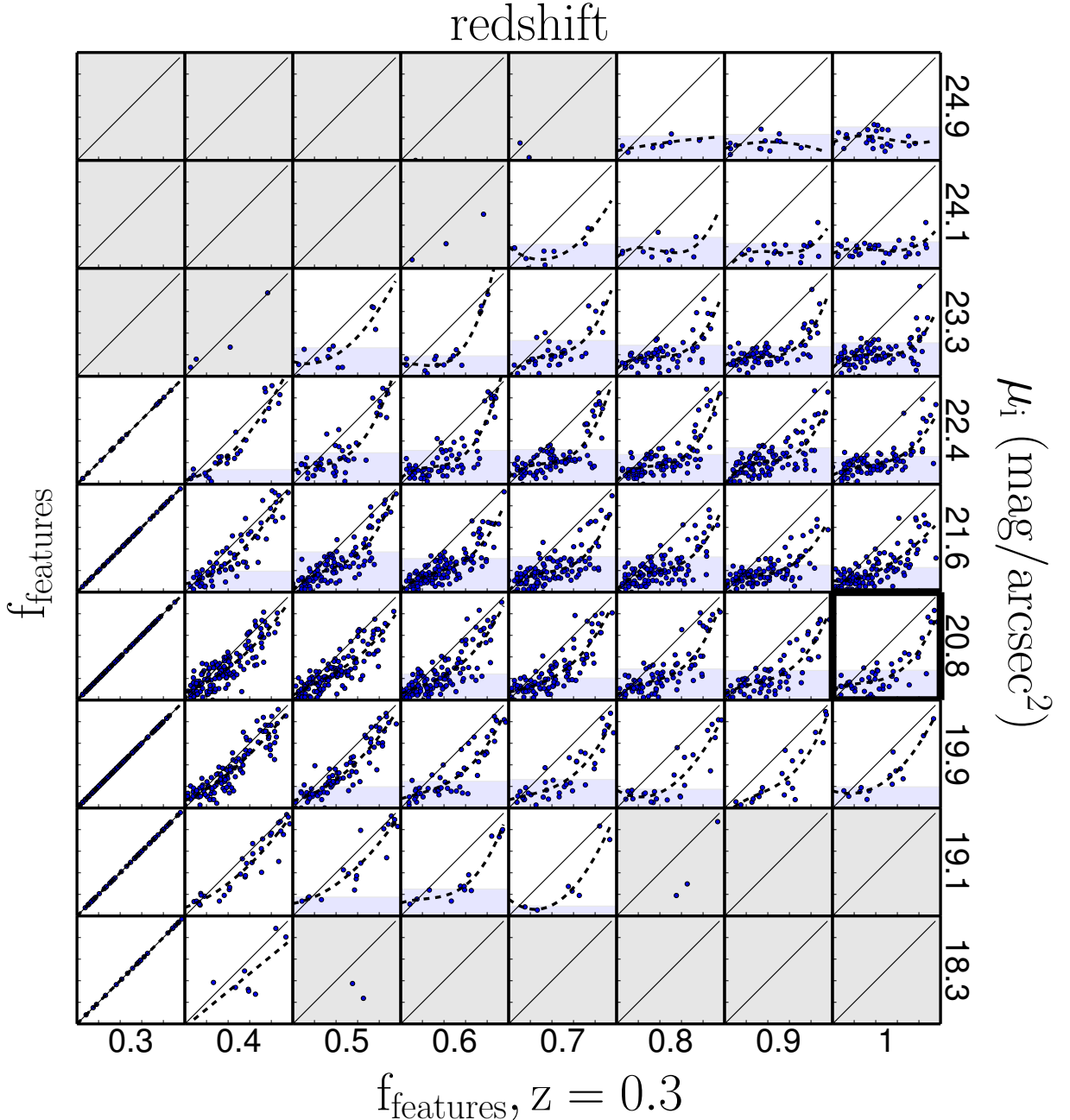


Figure 5.2 Effects of redshift bias in 3,449 images in the FERENGI sample. Each point in a given redshift and surface brightness bin represents a unique galaxy. On the y -axis in each bin is the f_{features} value of the image of that galaxy redshifted to the value corresponding to that redshift bin. On the x -axis is the f_{features} value of the image of the same galaxy redshifted to $z = 0.3$. The dashed black lines represent the best-fit polynomials to the data in each square. The solid black line represents $f_{\text{features},z} = f_{\text{features},z=0.3}$. Regions in which there is a single-valued relationship between f_{features} at high redshift and at $z = 0.3$ are white; those in which there is not are blue, and those with not enough data ($N < 5$) are grey. A larger version of the bin outlined at $z = 1.0$ and $20.3 < \mu < 21.0$ (mag/arcsec²) is shown in Figure 5.3.

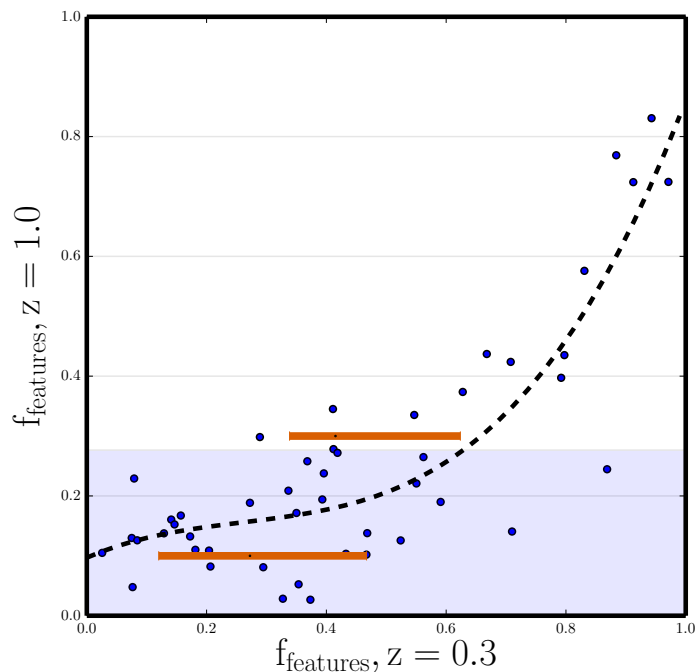


Figure 5.3 A larger version of the dark-outlined square in Figure 5.2, containing FERENGI galaxies that have been artificially redshifted to $z = 1.0$ and have surface brightnesses between $20.3 < \mu < 21.0$ (mag/arcsec 2). The orange bars represent the inner 68% (1σ) of the uncorrectable f_{features} quantiles, which are used to compute the limits on the range of debiased values.

of the dark outlined bin in Figure 5.2). This figure shows that if the value of f_{features} measured for a galaxy at $z = 1$ is particularly low, there is a wide range that f_{features} could have been if measured at $z = 0.3$. Therefore, a low measured value of f_{features} at high redshift could represent two morphological types of galaxies: 1) The galaxy has no distinguishable features and may be classified as a smooth elliptical, or 2) the galaxy *does* have features, but these have become blurred and too difficult to detect at high redshift.

It is important to identify such regions of surface brightness/redshift/ f_{features} space since vote fractions cannot be confidently corrected to a single value for galaxies in these regions. The criteria for determining whether a region of this space is single-valued, and therefore correctable, is as follows: In each surface brightness and redshift bin, the relationship between $f_{\text{features},z}$ and $f_{\text{features},z=0.3}$ is modelled by fitting the data with polynomials of degrees n=3,2, and 1, and using the best formal fit out of the three as measured by the sum of the residuals. These fits are shown as the dashed black lines in Figures 5.2 and 5.3. Flat regions of the bins are areas in which there is *not* a clear single-valued relationship between $f_{\text{features},z}$ and $f_{\text{features},z=0.3}$. This is quantified by measuring the slope of the best-fit polynomial to the vote fractions; regions of the bins with a slope less than 0.4 are considered *not* one-to-one, and therefore $f_{\text{features},z}$ cannot be boosted to its $f_{\text{features},z=0.3}$ value. These are colored blue in Figure 5.2 and are referred to as the *lower limit* sample, because the most stringent correction available is that the weighted f_{features} is a lower limit to the true value.

The unshaded regions of Figure 5.3 define discrete ranges of redshift, surface brightness, and f_{features} within which a galaxy must lie in order for the debiased vote fraction to be confidently applied. While the appropriate correctable regions were defined as discrete bins, the true correctable region is assumed to be a smooth function of z , μ , and f_{features} . To define this smooth space, a convex hull was calculated to enclose the correctable and lower-limit FERENGI galaxies in the $z - \mu - f_{\text{features}}$ space (see Figure 5.4). The space defined by this hull was used to ultimately separate the GZH galaxies into correctable samples (those for which a correction to f_{features} can confidently be applied, see next section) and lower-limit samples (those for which a single-valued correction cannot be applied). The final categorization of the GZH sample, split by imaging survey, is shown in Table 5.1.

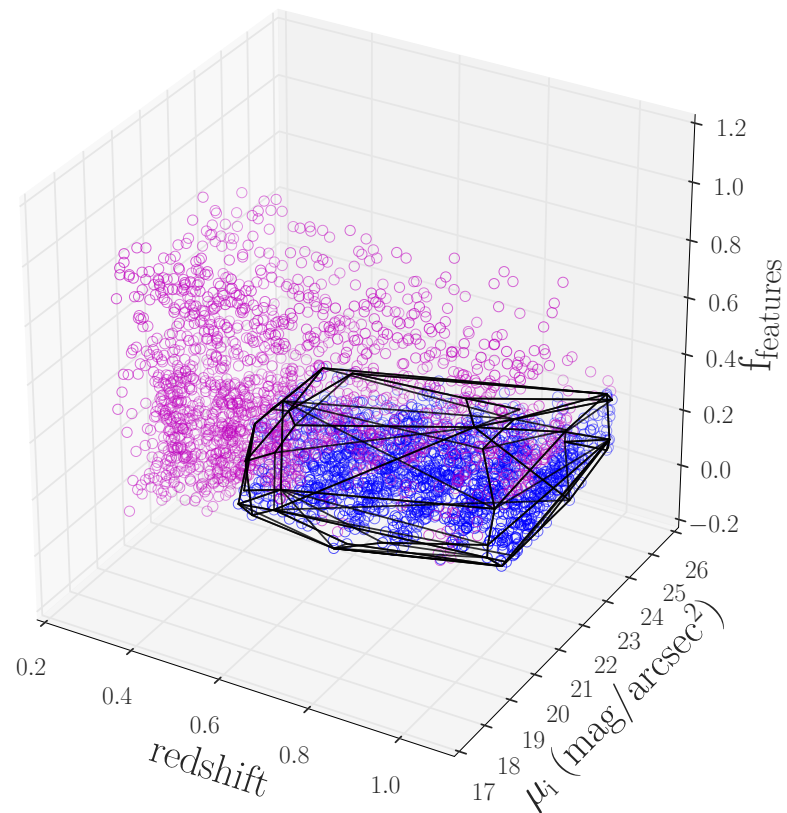


Figure 5.4 The final separation of the correctable and lower-limit samples in redshift/surface brightness/ f_{features} space. **Pink** points are all FERENGI galaxies in the **unshaded** regions of Figure 5.2. **Blue** points are all FERENGI galaxies in the **blue shaded** regions of Figure 5.2. The solid black line is the convex hull which encloses the uncorrectable points and defines the region of the lower-limit sample.

Table 5.1 Number of correctable galaxies for the top-level task in GZH, split by *HST* survey.

	Correction type	AEGIS	COSMOS	GEMS	GOODS-N 5-epoch	GOODS 5-epoch
correctable	0	2,908	21,169	2,802	1,459	1,120
lower-limit	1	833	5,169	1,021	1,377	1,200
no correction needed ($z \leq 0.3$)	2	955	10,870	1,175	415	400
not enough information (NEI)	3	2,677	43,058	3,559	2,077	2,100
no redshift information	4	1,134	4,688	530	687	1,000
total		8,507	84,954	9,087	6,015	5,117

For the “lower limit” galaxies, since a single debiased f_{features} value cannot be confidently assigned, a *range* of debiased values is estimated. In each z, μ bin in Figure 5.2, the spread of intrinsic values of $f_{\text{features}, z=0.3}$ for five quantiles of observed f_{features} is computed - these are denoted by the gray lines in the close-up Figure 5.3. The range of intrinsic values of f_{features} is defined by the upper and lower 1σ limits, enclosing the inner 68% of the data; this is represented by the orange bars in Figure 5.3. For any galaxy which cannot be directly debiased, these ranges are used to denote the upper and lower limits on the expected values $f_{\text{features}, z=0.3}$ as a function of the observed f_{features} .

5.3.2 Computing debiased f_{features} for the “correctable” sample using the ζ equation

For the “correctable” sample of simulated FERENGI galaxies, an equation is derived to model the dropoff in f_{features} with redshift for each galaxy. Such a model is assumed to have the following criteria: (1) For a given galaxy, f_{features} should decrease relative to its $f_{\text{features}, z=0.3}$ as redshift increases. (2) The corrected f_{features} value must be contained within 0 and 1, since it is a fraction. (3) The degree of dropoff may depend on the surface brightness of the galaxy. Given these three assumptions, a simple exponential function was derived:

$$f_{\mu, z} = 1 - (1 - f_{\mu, z=0.3})e^{\frac{z-z_0}{\zeta}} \quad (5.4)$$

where $f_{\mu, z=0.3}$ is the vote fraction at the lowest redshift in the artificially-redshifted FERENGI sample ($z_0 = 0.3$). ζ is a parameter that controls the rate at which f_{features} decreases

with redshift.

Equation 5.4 is then fit to each galaxy in the “correctable” FERENGI sample, and ζ is measured for each. Figure 5.5 shows the best fit equations for 16 galaxies, and the ζ corresponding to the best fit is displayed with each galaxy. As it was assumed that surface brightness likely plays a role in the level of dropoff in f_{features} , and hence the value of ζ which controls this dropoff, it is assumed that ζ follows a simple linear dependence with surface brightness:

$$\log_{10}(\hat{\zeta}) = \zeta_0 + (\zeta_1 \times \mu), \quad (5.5)$$

where $\hat{\zeta}$ is the correction factor applied to each galaxy. Figure 5.6 shows the relationship between the derived ζ values and the surface brightness μ of the FERENGI galaxies, which is fit with equation 5.5. The best-fit parameters to this linear fit from least-squares optimization are $\zeta_0 = 0.50$, $\zeta_1 = -0.03$. Interestingly, only a very weak surface brightness dependence is detected. It is difficult to determine from these data whether the weak detection is due to a true lack of dependence, or insufficient data (only 28 galaxies had sufficient data to accurately measure ζ).

Using the ζ parameters measured in the FERENGI sample, a final debiased correction equation is derived to correct the f_{features} vote fractions in the HST data:

$$f_{\text{features,debiased}} = 1 - (1 - f_{\text{features,weighted}}) e^{\frac{-(z-z_0)}{\hat{\zeta}}} \quad (5.6)$$

where $f_{\text{features,weighted}}$ is the weighted vote fraction, and $f_{\text{features,debiased}}$ is bounded between $f_{\text{features,weighted}}$ and 1.

5.3.3 Results and the NEI sample: limitations of the ferengi simulated data

- show table of HST sample breakdown 5.1
- show how above method only works for HST galaxies with z/μ corresponding to ferengi space 5.8
- discuss why ferengi can’t completely replicate mu distribution of HST (cite Karen response to referee)

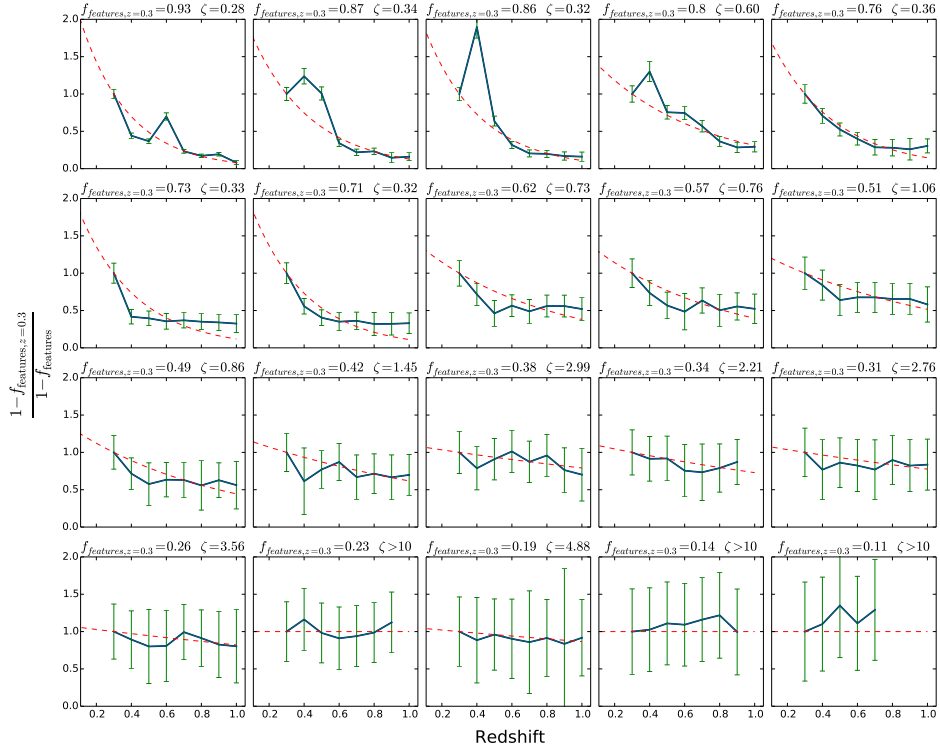


Figure 5.5 Behaviour of the normalised, weighted vote fractions of features visible in a galaxy (f_{features}) as a function of redshift in the artificial FERENGI images. Galaxies in this plot were randomly selected from a distribution with evolutionary correction $e = 0$ and at least three detectable images in redshift bins of $z \geq 0.3$. The displayed bins are sorted by $f_{\text{features},z=0.3}$, labeled above each plot. Measured vote fractions (blue solid line) are fit with an exponential function (red dashed line; Equation 5.4); the best-fit parameter for ζ is given above each plot.

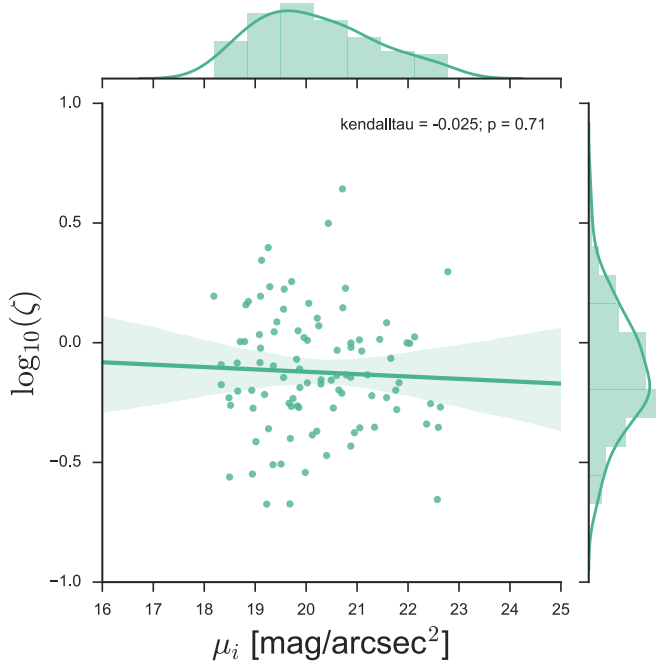


Figure 5.6 All fits for the FERENGI galaxies of the vote fraction dropoff parameter ζ for f_{features} as a function of surface brightness. This includes only the simulated galaxies with a bounded range on the dropoff ($-10 < \zeta < 10$) and sufficient points to fit each function (28 original galaxies, each with varying images artificially redshifted in one to eight bins over a range from $0.3 \lesssim z_{\text{sim}} \lesssim 1.0$).

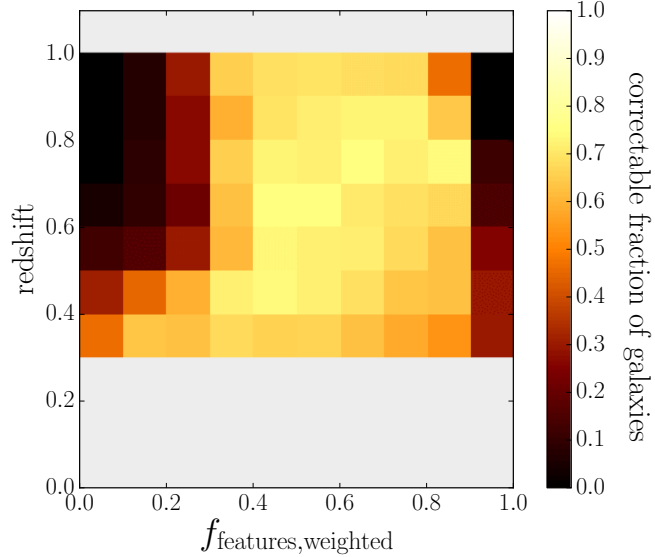


Figure 5.7 Histogram showing the fraction of galaxies that have a finite correction for the debiased vote fractions $f_{\text{features,debiased}}$ as a function of f_{features} and redshift. The parameter space for corrections is limited to $0.3 \leq z \leq 1.0$ due to the sampling of the parent SDSS galaxies and detectability in the FERENGI images.

- discuss limits shown in 5.7

5.4 Ferengi 2: using simulated images to measure incompleteness in disk fraction as a function of redshift and surface brightness

In the previous section I described how we used the simulated FERENGI images to measure the redshift/surface brightness dependence on f_{features} , and applied the measurements towards a correction factor to the vote fractions directly. In this section I will describe the motivation, selection, and application of a second set of FERENGI images used to measure and correct for the incompleteness in *number* of disks detected as a function of redshift and surface brightness, used in the work described in Chapter 6.

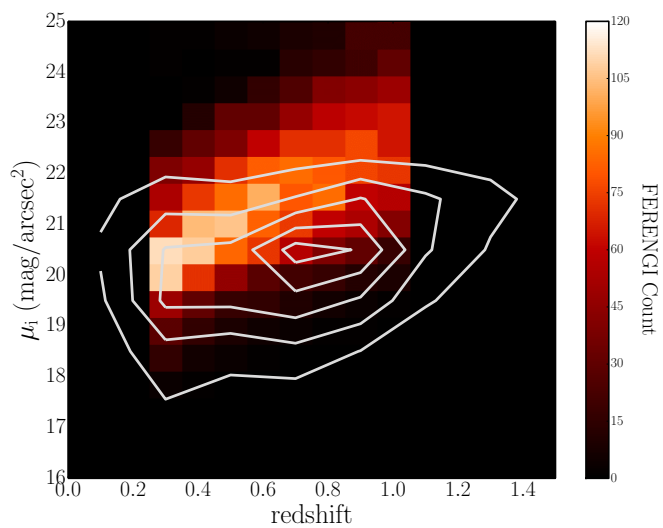


Figure 5.8 Surface brightness as a function of redshift for 3,449 FERENGI images and the 102,548 `main` galaxies with measured μ and z values. The colour histogram shows the number of FERENGI images as a function of μ and z_{sim} . White contours show counts for the galaxies in the `main` sample, with the outermost contour starting at $N = 1500$ and separated by intervals of 1500.

5.4.1 The Ferengi 2 Sample

The creation of a second set of FERENGI images was motivated by the scientific goal of measuring the redshift evolution of the fraction of red disk galaxies using the Galaxy Zoo: Hubble dataset. This project is described in full in Chapter 6, but the reasons requiring a new set of simulated images will be described briefly here. First, as described in the previous section, the analysis of the first FERENGI set revealed that, for a large area of $z-\mu$ parameter space, galaxies with low measured values of f_{features} could not be corrected to a point that could clearly distinguish them as disks with washed-out features or ellipticals. Due to this limitation, any measurement of the number of disk galaxies in a given redshift interval can only be reported as a *lower-limit* to the true value. The difference in the measured lower-limit and the true number of disks is what we will refer to as the *incompleteness* in number of disks detected.

It is possible, then, to use the FERENGI images to measure this incompleteness by measuring the number of disks detected at a given redshift, and comparing to the number of disks detected out of the same galaxies at the lowest redshift (this would be considered the true, or intrinsic, number of disks.) The details of this approach will be described in the next section. A complication specific to this project is that the number of disks will be ultimately used to compute the *red disk fraction*, that is, the ratio of the number of red disks to all disks, as a function of redshift. It is then necessary to measure the level of incompleteness for both red and blue galaxies separately, to calculate this fraction most accurately.

The color separation method for the *HST* galaxies in Chapter 6 uses NUV, r, and J magnitudes. To separate the FERENGI sample of galaxies into red and blue samples in the same way, these magnitudes are required. In the first set, however, only 44 of the 288 galaxies had these data available, which were not enough to properly measure any incompleteness, especially after binning the data further in surface brightness and redshift. So, a larger set of galaxies to be artificially redshifted, all which had the aforementioned data necessary to separate by color, was required.

This set of new galaxies to be put through the FERENGI code, hereafter referred to as the FERENGI 2 sample, was selected as follows: All candidates were pulled from a parent sample of all SDSS galaxies which had previously been classified in GZ2. As discussed in Section 5.2, only galaxies with redshifts below $z < 0.013$ were able to be redshifted

the full simulated redshift range $0.3 < z < 1.0$, so a redshift cut was implemented of $z < 0.013$. These galaxies were cross-matched with catalogs from GALEX (Martin et al., 2005) for NUV magnitudes and 2MASS (Skrutskie et al., 2006) for J magnitudes. 1,435 galaxies fit these criteria.

Bulk SDSS u, g, r, i, and z-band fits images were then downloaded for all 1,435 galaxy candidates ⁴. Cutouts were made for each galaxy, using the 90% r-band petrosian radius to set the size of the cutout (PETROR90_R). The default prescription used was to define the edges as 2.5*PETROR90_R, measured from the galaxy as the center. If the galaxy was within this distance from the edge of the bulk fits image, 2.0*PETROR90_R was used. Cutouts were not made for galaxies within this distance from the edge, both to ensure the full galaxy was visible in all cutouts in the sample, and to avoid over-zooming the image. 187 galaxies were thus removed from FERENGI2; an example of such a galaxy “too close” to the edge of the edge is shown in Figure 5.9.

While all $78 z < 0.013$ galaxies from the original FERENGI sample were successfully simulated to a minimum redshift of $z_{sim} = 0.3$, this was not always true for the FERENGI2 candidates. Redshift of the source galaxy is the largest factor in determining the minimum possible simulated redshift, but other factors including the size of the psf and physical size of the source galaxy also come into play. All 1,248 candidates were then put through FERENGI at only the lowest redshift $z_{sim} = 0.3$ to begin, and each image was visually inspected to determine whether the code succeeded. 312 “failures” were detected; two examples are shown in Figure 5.10. The remaining 936 “successes” were then artificially redshift the full range of $0.3 < z < 1.0$ in increments of $dz = 0.1$; these make up the final FERENGI2 sample of 7,488 images of 936 galaxies redshifted 8 times. A single evolution factor, rather than a range, of $e = 1$ was applied to all images. This value was chosen by analyzing the spectra template models of Brinchmann et al. (2004), which showed that the most typical galaxies evolve in brightness by one magnitude per redshift. Example images are shown in Figure 5.11

⁴ <http://data.sdss3.org/bulkFields>

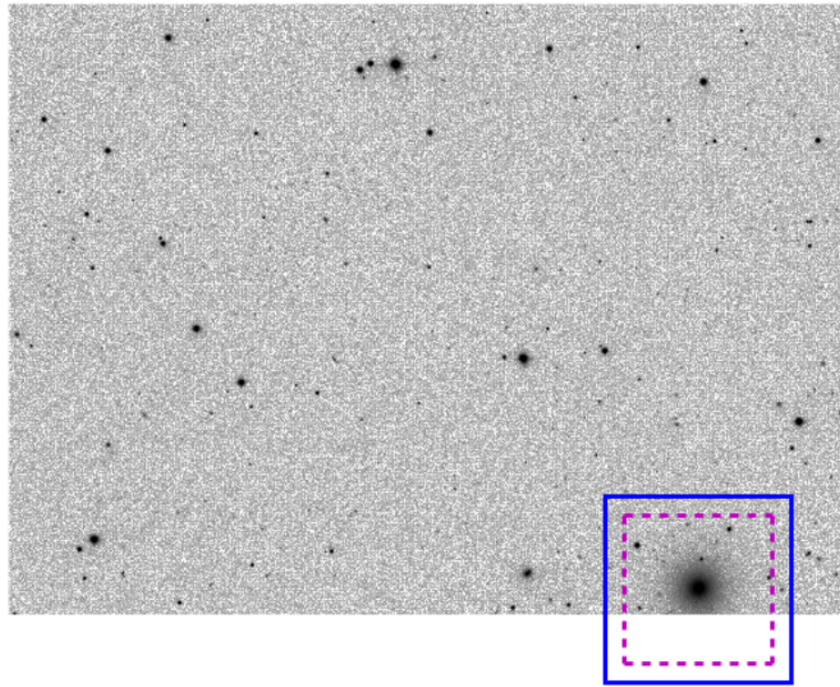


Figure 5.9 Example of a galaxy overlapping the edge of the SDSS frame. Shown is the bulk r-band fits image for SDSS DR12 run 3903, camcol 6, and field 60. The boxed-in galaxy (SDSS DR12 objid 1237662239079268544) is too close to the edge of the image to create a cutout that encloses the entire galaxy. The pink dashed box indicates a cutout size of $2 \times \text{PETRO}R_{90,R}$, the blue solid line indicates a cutout size of $2.5 \times \text{PETRO}R_{90,R}$.

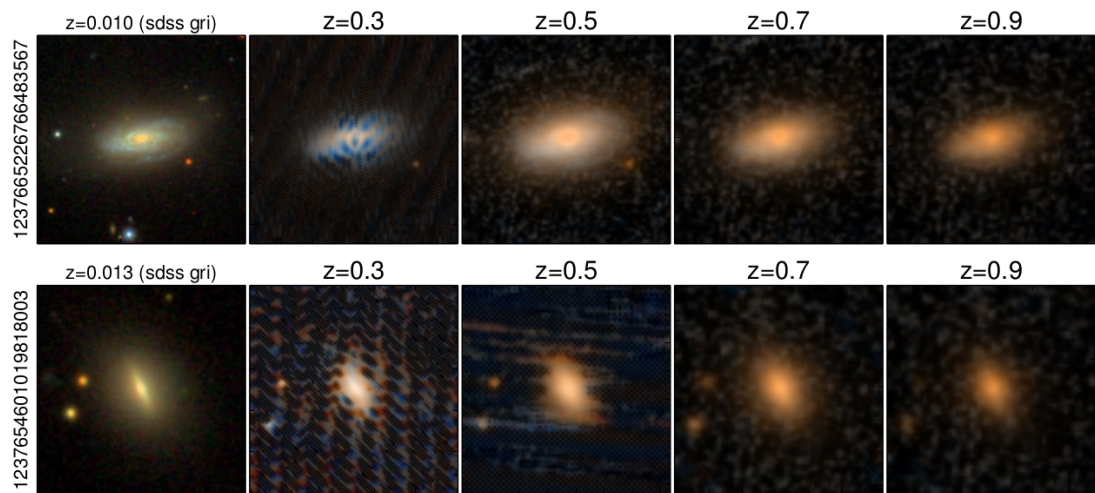


Figure 5.10 Examples of two galaxies whose minimum simulated redshifts in FERENGI were larger than $z_{sim} = 0.3$. These were detected via visual inspection and removed from the final FERENGI2 sample.

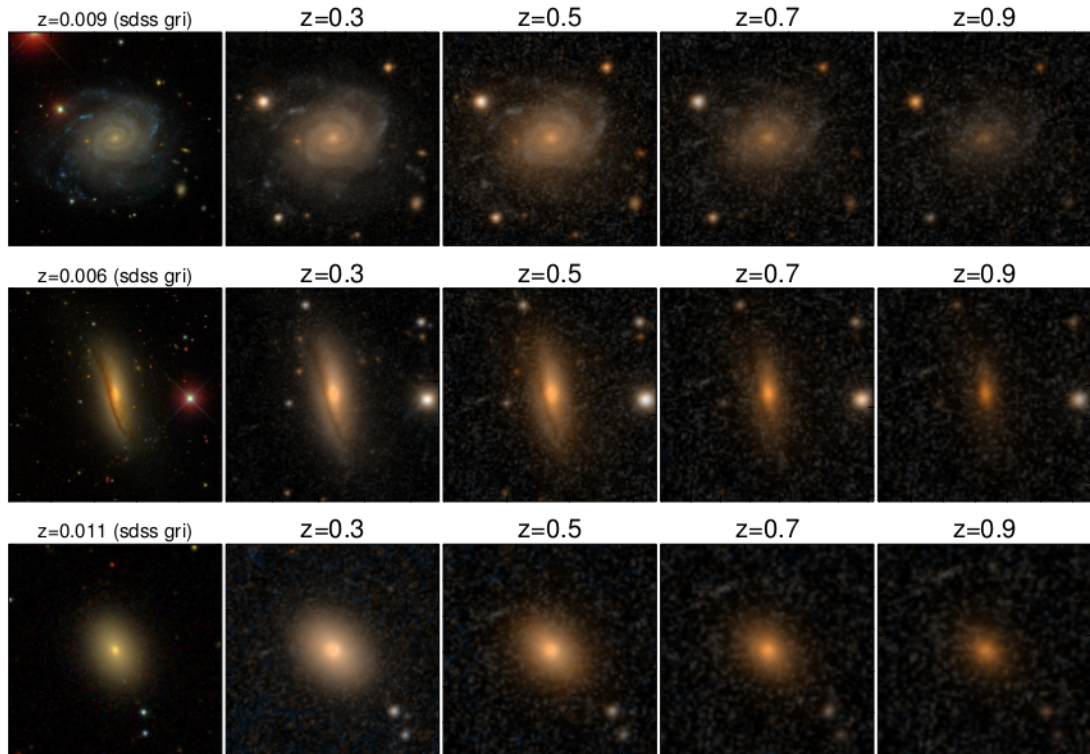


Figure 5.11 Examples of FERENGI2 galaxies. The left is the original gri-composite image of the source galaxy. Images on the right are simulated output from the FERENGI code. Only four of the eight simulated redshifts are shown in the interest of space.

Chapter 6

GZH red disk fraction

It is well known that most galaxies tend to exist in one of two populations: blue, late-type disks exhibiting active star formation, and red, early-type ellipticals showing little to no signs of recent star formation (Strateva et al., 2001; Baldry et al., 2004). The division between the two color populations is quite distinct when visually represented on a color-magnitude (CMD) or color-color diagram. As shown in the CMD in Figure 6.1, galaxies tend to populate in one of two regions: the “red sequence” in the upper band, which contains predominantly early-type galaxies, and the “blue cloud” in the lower, containing mostly late-type spirals. This bimodality in the color-morphology relationship of galaxies has been so widely accepted that color is often used as a proxy for morphological classification in large samples of galaxies (e.g. Cooray (2005); Lee & Pen (2007); Salimbeni et al. (2008); Simon et al. (2009)), where expert visual classification is not feasible on such scales (see also: Chapter 2), while color measurements are more easily available.

The relatively tight correlation suggests an evolutionary link between a galaxy’s dynamical history (traced by its morphology) and stellar content (traced by its color). In the simplest interpretation, it could be deduced that galaxies tend to begin their lives as young, star-forming disks, until some mechanism (secular or external) causes star-formation to cease while the galaxy simultaneously undergoes a morphological transformation from disk to spheroidal.

The advent of larger surveys and more reliable methods for measuring morphology (independently of color) has allowed for more nuanced interpretations of the simple

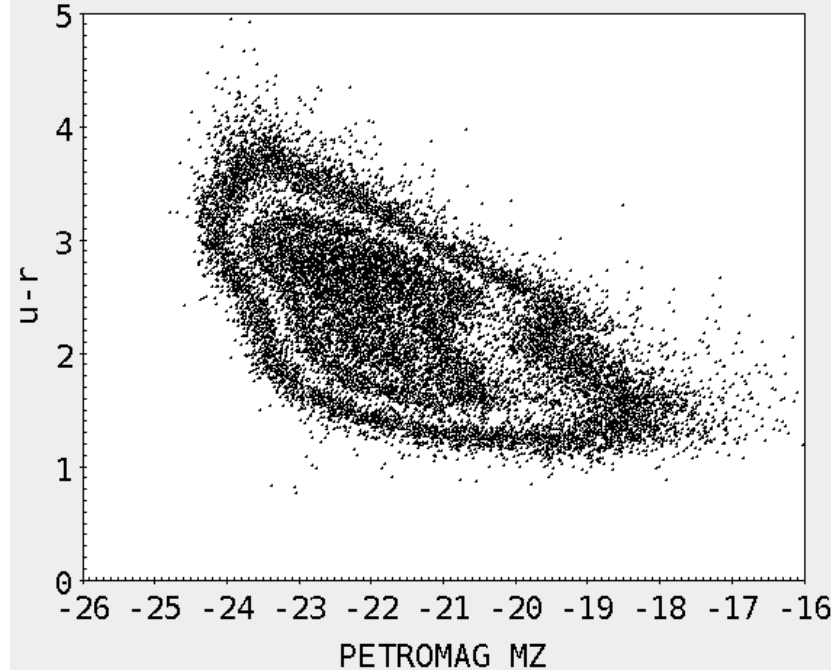


Figure 6.1 cmd figure

model. For instance, the degree of incompleteness in the color-morphology relationship is now much more realized, with the recent identifications of significantly large samples of red spirals and blue ellipticals. Using morphological classifications from GZ1, Masters et al. (2010) found 6% of a sample of ~ 5000 spirals to be red; similarly, Schawinski et al. (2009a) found 6% of early-type galaxies to be blue. The existence of these objects may represent transition phases in the pathway from the blue cloud to the red sequence, and also give insight into what processes may quench or initiate star-formation without inducing a morphological change, or visa versa.

Another probe for understanding the transition from blue cloud to red sequence is the “green valley”, the intermediate region between the two. In addition to the ellipticals in the blue cloud and spirals in the red sequence, galaxies of all types residing in the green valley were thought to represent the transition stages of this evolutionary pathway. The intermediate colors in this region indicate a recent quenching of star-formation (Martin et al., 2007; Salim et al., 2007), and the dearth of galaxies here (as compared to the high populations in the red sequence and blue cloud) initially suggested that the quenching

process initiating transition across the CMD is very rapid.

A closer look at the populations within the green valley show that the processes causing galaxies to evolve from the blue cloud to red sequence may be very different. Schawinski et al. (2009a) studied the morphological distribution (measured by the GZ1 project) of ~ 4000 green-valley galaxies, finding that late-type and early-types likely go through two different evolutionary tracks. For late-types, the quenching process is gradual, and initiated by a cutoff of a gas reservoir. Galaxies quenched recently in this way would populate the green valley at $z = 0$, and those which quenched at an earlier time would be currently identified as red passive disks. Whether these red disks continue to evolve into spheroidals via some process after the initial quenching is unclear from a local Universe analysis. For early-types, the quenching is rapid and probably external and violent, thus triggering the morphological change from disk to spheroidal.

Analysis of the color-morphology relationship in the local Universe has revealed a close but imperfect bimodality as well as proposed mechanisms by which galaxies undergo different quenching processes, driving their evolution along the CMD. Even more may be revealed by studying the different populations as a function of cosmic time, which is becoming more possible with the data from large high-redshift surveys such as COSMOS and deep imaging via HST-ACS. It has been established now, for instance, that the bimodality does exist out to $z \sim 1$ (Bell et al., 2004; Cirasuolo et al., 2007; Mignoli et al., 2009) and possibly beyond (Giallongo et al., 2005; van Dokkum et al., 2006; Franzetti et al., 2007; Cassata et al., 2008). What requires further study is how exactly the proportions change at different epochs.

6.0.2 Quenching Mechanisms

An isolated galaxy will eventually cease to form new stars as it naturally exhausts its limited supply of gas. The time-scale for complete consumption can be estimated from the amount of gas in a typical galaxy and the rate at which it is consumed through star formation: $\tau \sim M_{\text{gas}} / \dot{M}_{\text{gas}}$ (Larson, R.B., Tinsley, B.M. and Caldwell, 1980), and is expected to range from 1-3 Gyr. Most galaxies do not exist in such isolation; the exchange of matter in the galaxy due to its surroundings can disrupt and often accelerate the depletion of a galaxy's gas reservoir. Quenching is defined as any process

which drives the shutting-down of star formation in this way. This section will introduce different proposed quenching mechanisms, some of which are internal (driven by the galaxy's structure or components), or external (driven by direct influence of the surrounding environment).

Ram Pressure Stripping

As a galaxy moves through the intracluster medium (ICM), it experiences ram pressure $P_{ram} = \rho_e v^2$, where ρ_e is the density of the ICM and v is the velocity of the galaxy (Gunn & E. and Gott, III, 1972). The force per area required to hold gas onto the traveling galaxy is $F/A = 2\pi G\sigma_s\sigma_g$, where σ_s and σ_g are the star and gas surface densities, respectively. If a galaxy is moving fast enough, or the ICM density is large enough, the ram pressure can exceed this force and consequently rip the gas from the galaxy; this process is known as ram pressure stripping. Evidence of this effect is seen observationally in asymmetries of the disk in spirals (a common example is NGC 4402, which has a bowed appearance and a one-sided concentration of dust, believed to be the effects of the galaxy struggling to hold onto gas on the outer regions of the disk) and truncated radial density profiles. Simulations (Steinhauser et al., 2016) show that extreme cases of ram pressure stripping can completely strip a galaxy of its cold gas, causing a rapid quenching on timescales of a few hundred Myr. More mild cases, on the other hand, can actually temporarily increase star formation, which quickly uses up the available cold gas, and eventually quenches the galaxy on timescales similar to natural isolation, ~ 1 Gyr. Fillingham et al. (2016) find a mass dependence on the efficiency of this process: they find RPS to be very efficient and rapid for galaxies $M_* = 10^{8-9} M_\odot$ for a range of halo host properties, suggesting RPS may be the dominant quenching mechanism for low-mass galaxies.

Strangulation

Even if the ram pressure exerted by the ICM is not strong enough to completely remove all of the gas from a galaxy, it may be just strong enough to strip the outer hot gas which would have otherwise cooled and replenished the cold gas reservoir. This process is defined as strangulation, where star formation ceases after the initial cold gas is used up (Larson, R.B., Tinsley, B.M. and Caldwell, 1980). This process can be sped up even

more if the ram pressure compresses the cold gas, causing an increased bursting of star formation, depleting it completely on a time scale of $\sim 1\text{-}2\text{Gyr}$ (Kawata & Mulchaey, 2007).

Harassment

Mass quenching

AGN feedback

Mergers

6.1 Sample Selection

info to include: cross match with ultravista for rest-frame colors, volume limit, morphological cuts (pfeatures, pclumpy, pedgeon)

6.2 Galaxy Classification: Identifying the Passive Population

To classify the galaxies as quiescent or star-forming, a method similar to that described by Ilbert et al. (2013) (hereafter I13) was used, which implements a rest-frame $NUV-r^+$ versus r^+-J diagnostic. Here are some reasons these colors are great ($NUV-r:$) (Arnouts et al., 2007; Salim et al., 2005; Wyder et al., 2007), (Martin et al., 2007)

The demarcation line to separate the quiescent and active populations at $z = 1$ is adopted from I13, which defines the quiescent galaxies as those which satisfy: $M_{NUV} - M_{r^+} > 3(M_{r^+} - M_J) + 1$ and $M_{NUV} - M_{r^+} > 3.1$. I13 applies this criteria to all galaxies in a range of $0.2 < z < 3$, although it performs best at separating the two populations in the redshift bin $0.7 < z < 1.2$, where $> 98\%$ of galaxies identified as quiescent exhibited star formation rates less than $\log(SFR) = -11$ (see Figure 3 of I13). Therefore this work uses the I13 separation criteria at $z = 1$, and computes the evolution of the demarcation lines as a function of redshift to $z = 0$.

The evolution of $r - J$ and $NUV - r$ colors was measured using a stellar population synthesis model from Bruzual & Charlot (2003). An instantanious-burst model (ssp)

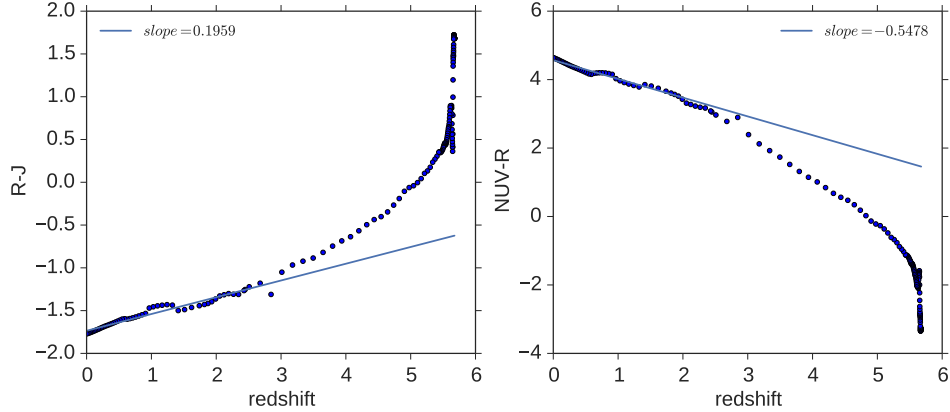


Figure 6.2 Evolution of colors using stellar population synthesis models. Galaxy was assumed to have formed at $z = 6$ for plotting purposes.

was chosen from the Padova1994 track to represent the color evolution of a passively evolving galaxy, with a metallicity $Z = 0.008 = .4Z_{\odot}$, which is the typical metallicity of passive galaxies with mass $9 < \log(M_*/M_{\odot}) < 10$ (Peng et al. (2015), Figure 2a), chosen to correspond to the median mass of the sample ($\log(M_*/M_{\odot}) = 9.7$). Figure 6.2 shows the evolution of the two colors as a function of redshift, where the single starburst at $t = 0$ was placed at $z = 6$. A linear relationship was fit to the data within the range $0 < z < 2$, and the slope was used to redefine the demarcation lines in five redshift bins: one with central value $z = 0.007$ (used to classify the SDSS ferengi2 sample), and four with central values $z = [0.30, 0.50, 0.70, 0.90]$ with widths $\Delta z = 0.2$. The quiescent galaxies are thus defined in these bins as those that satisfy:

$$M_{NUV} - M_{r+} > 3.1 + a_1(z) \text{ and } M_{NUV} - M_{r+} > 3(M_{r+} - M_J + a_2(z)) + a_1(z) + 1 \quad (6.1)$$

where $a_1(z) = [0.54, 0.38, 0.27, 0.16, 0.05]$ and $a_2(z) = [0.19, 0.14, 0.10, 0.06, 0.02]$.

6.3 Using Ferengi2 to correct for incompleteness in the red disk fraction

described in previous section that it's difficult or impossible to disentangle whether a small vote fraction of f_{features} corresponds to galaxies which are intrinsically smooth, or

whose features have been washed out at high redshift. So while we can't correct the vote fraction for unique galaxies, we *can* estimate the *number* of disk galaxies we would fail to detect at a given redshift.

To account for this incompleteness in disk detection, a correction factor ξ is applied. This is defined as the number of disks detected divided by the true number of disks expected to exist in a given redshift interval: $\xi(z) = N_{\text{detected}}/N_{\text{true}}$. Acknowledging that the completeness in disk detection may depend on galaxy color, the corrected red disk fraction can be calculated as:

$$f = \frac{N_{RD} \times \xi_{red}^{-1}}{N_{RD} \times \xi_{red}^{-1} + N_{BD} \times \xi_{blue}^{-1}} \quad (6.2)$$

If there is no color bias in disk detection, $\xi_{red} = \xi_{blue}$, and this term cancels out, leaving the fraction unchanged. If there is a bias, however, the ξ terms do not cancel, and the incompleteness in disk detection could have a large effect on the red disk fraction. Therefore a careful measurement of ξ is estimated for both red and blue disk galaxies using the FERENGI2 set of simulated images.

FERENGI2 is the set of images created from 936 nearby ($z < 0.01$) galaxies that were artificially redshifted to 8 redshifts between $z = 0.3$ and $z = 1$, giving a total of 7,488 simulated images (the sample is described in detail in Chapter 5). The images were classified in Galaxy Zoo using the same decision tree as used for Galaxy Zoo Hubble. 134 highly inclined disk galaxies were removed from the sample by excluding any with $N_{edgeon} > 20$ and $f_{\text{not edge-on}} \geq 0.6$, using the vote fraction associated with the real galaxy image measured in GZ2. This cut was shown in Chapter 3 to correlate well with inclination angle $\cos(a/b) < 67^\circ$. This was to exclude those which may be mis-classified due to dust-reddening (see section 6.1). Using the NUV-J-R selection method described in section 6.2, the remaining sample was divided into a set of red sequence galaxies (259 per redshift bin) and blue cloud (543 per each redshift bin), shown in Figure 6.3.

The completeness values $\xi_{red}(z), \xi_{blue}(z)$ were then computed in varying bins of redshift for the red sequence and blue cloud galaxies separately. An example calculation of ξ_{blue} in the $z = 0.7$ bin is shown in Figure 6.4. Each point represents a FERENGI2 galaxy, where the y-axis indicates the value of f_{features} measured in the image redshifted to $z = 0.7$, and the x-axis indicates the value of f_{features} measured in the same galaxy redshifted to $z = 0.3$. Disk galaxies are identified as those for which $f_{\text{features}} \geq 0.3$. Since,

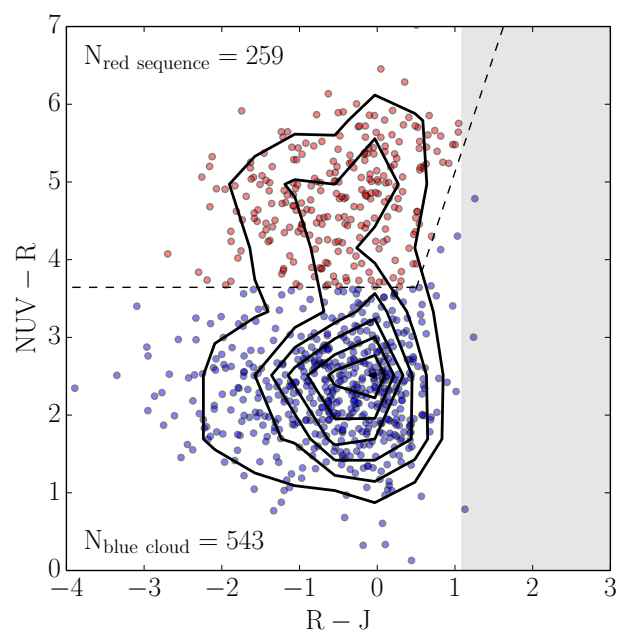


Figure 6.3 Separation of the quiescent population (red sequence) and active population (blue cloud) of the FERENGI2 sample.

on average, f_{features} decreases for the same galaxy as it is viewed at higher redshifts, the number of galaxies meeting this threshold is generally fewer at higher redshifts than lower redshifts. This is indicated by the dotted lines: galaxies to the right of the vertical dashed line at $f_{\text{features},z=0.3} = 0.3$ are identified as disks at $z = 0.3$; their sum is considered the “true” number of disks, N_{true} . Similarly, the galaxies above the horizontal line at $f_{\text{features},z=0.7} = 0.3$ are identified as disks at $z = 0.7$; their sum is the “detected” number of disks at $z = 0.7$, or N_{detected} . As obvious in the figure, N_{detected} is in general much lower than N_{true} , emphasizing the increasing difficulty in detecting features at higher redshifts. Their ratio is the completeness ξ ; in this example $\xi_{\text{blue}}(z = 0.7) = 0.61$, meaning only 61% of disks were detected at this redshift.

It was hypothesized that the completeness in disk detection may be a function of other parameters in addition to redshift. At fixed redshift, for example, it is reasonable to guess that features could be easier to detect galaxies that have higher mass, radius, or surface brightness. To test whether these parameters also impact the number of disks detected, the completeness was measured in fixed redshift bins as a function of surface brightness, effective radius, and mass. Surface brightness was measured using SExtractor calculations of `MAG_AUTO`, b/a and R_e measured in the I_{814W} band images, in the same way as described in Chapter 5. The effective radius used was the 50% `FLUX_RADIUS` converted in to kpc, and the masses used were the `MEDIAN` values calculated in the MPA-JHU catalog.

Figure 6.5 shows completeness as a function of redshift and surface brightness, for the red sequence and blue cloud galaxies. 8 redshift bins were further divided into bins of surface brightness with varying widths, where the sizes were chosen to satisfy that $N_{\text{detected}} + N_{\text{true}} \geq 10$ in each bin. This was chosen as a compromise between having a sufficient number of galaxies in each bin to compute the completeness fraction $\xi = N_{\text{detected}}/N_{\text{true}}$, and to have enough bins of surface brightness to measure a trend with confidence of completeness as a function of μ . Visual inspection of the data did not suggest any relationship between the two. To be sure, the data were fit to a linear function in each redshift bin (Figure 6.7). For each fit, a p-value representing a hypothesis test whose null hypothesis is that the slope is zero was computed. Only one reached the criteria $p < 0.05$, but with a low R^2 value of 0.28 which is not considered large enough to represent a good fit. This process was repeated using effective radius

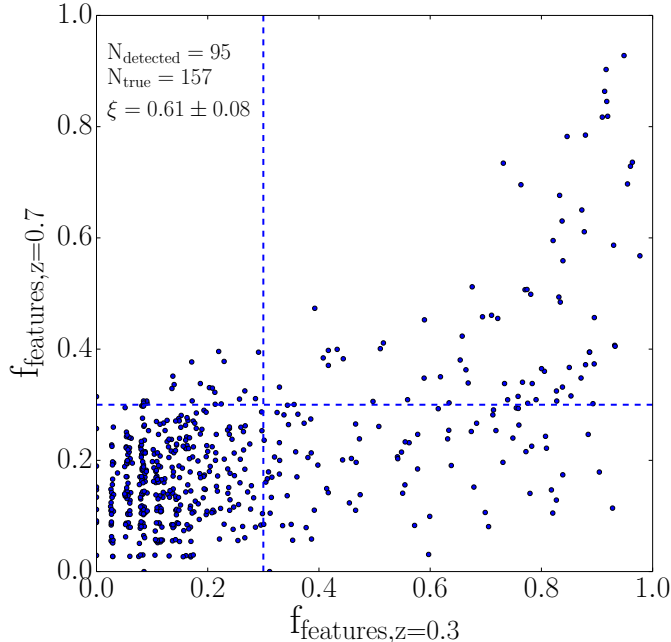


Figure 6.4 Example calculation of completeness ξ at redshift $z = 0.7$. Points represent FERENGI2 images classified in Galaxy Zoo. The y-axis corresponds to the value of f_{features} measured at the galaxy redshifted to $z = 0.7$, and the x-axis corresponds to the value of f_{features} measured at the galaxy redshifted to $z = 0.3$. On average, the f_{features} is lower at the higher redshift, indicating users on average have more difficulty identifying features in images at higher redshifts. The dotted lines correspond to $f_{\text{features}}=0.3$, the threshold above which a galaxy is considered to have a disk. Galaxies to the right of the vertical dashed line were identified as disks at the lowest redshift $z = 0.3$, the total number defined as N_{true} , the true number of disks. Galaxies above the horizontal dash line were identified as disks at the higher redshift $z = 0.7$, the total number defined as N_{detected} . The ratio $\xi = N_{\text{detected}}/N_{\text{true}}$ is the completeness value; in this example, only 61% of disks were detected at $z = 0.7$.

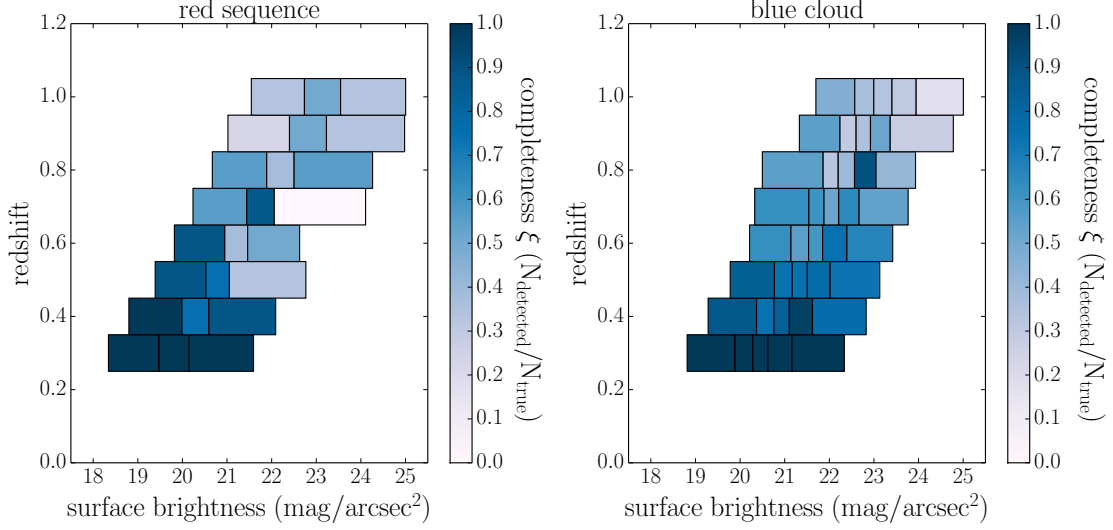


Figure 6.5 Completeness ξ as a function of redshift and surface brightness for red sequence (left) and blue cloud galaxies (right).

and mass as parameters, with the same results. Therefore only redshift was used as a parameter which impacted completeness value with confidence.

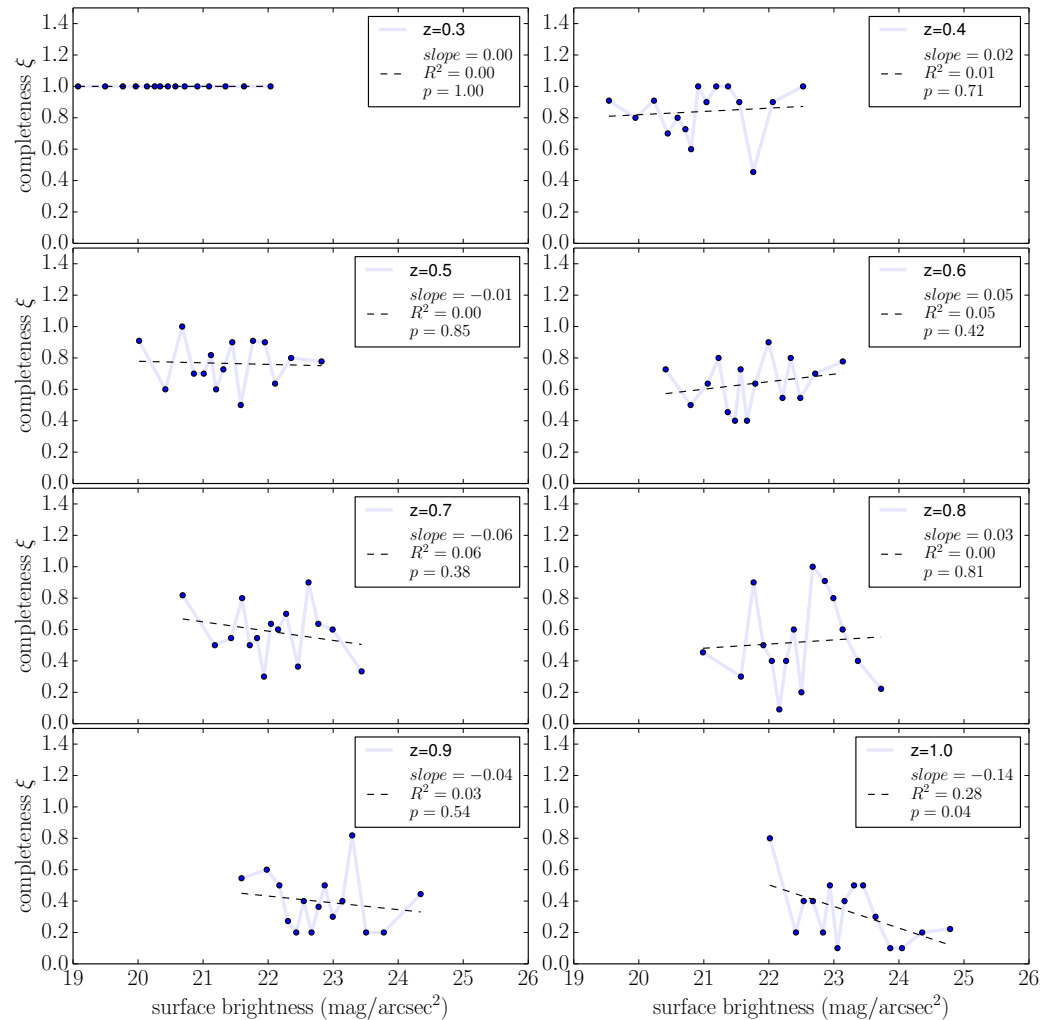
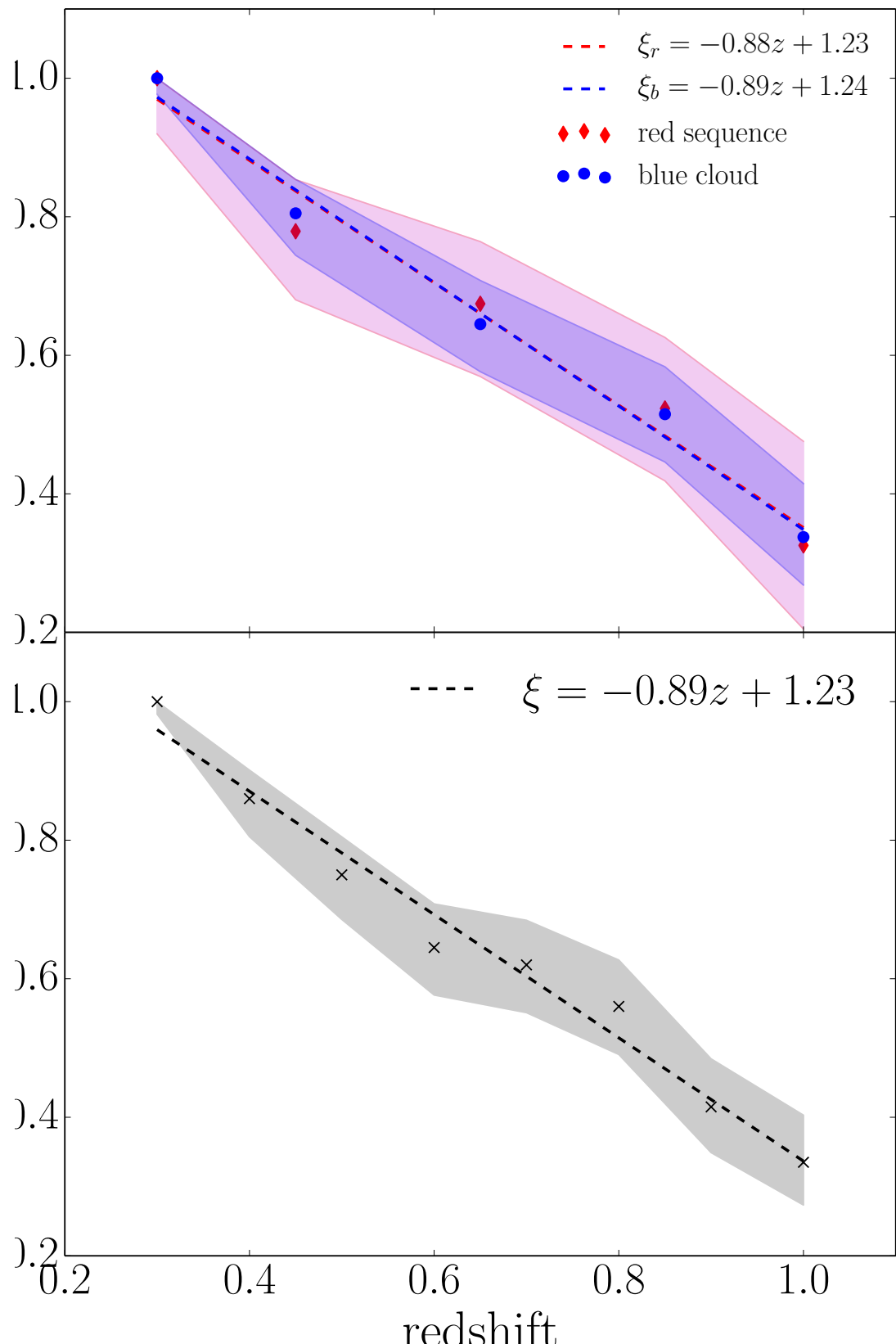


Figure 6.6 Completeness ξ as a function of redshift and surface brightness for red sequence (left) and blue cloud galaxies (right).



Chapter 7

Summary & Future Work

References

- AdelmanMcCarthy, J. K., Agüeros, M. A., Allam, S. S., et al. 2008, *The Astrophysical Journal Supplement Series*, 175, 297
- Anderson, D. P. 2002, *Commun. ACM*, 45, 56
- Ann, H. B., & Thakur, P. 2005, *The Astrophysical Journal*, 620, 197
- Antonini, F., Barausse, E., & Silk, J. 2015, arXiv:1506.02050
- Arnouts, S., Walcher, C. J., Le Fèvre, O., et al. 2007, *Astronomy and Astrophysics*, 476, 137
- Athanassoula, E. 1992, *Monthly Notices of the Royal Astronomical Society*, 259, 328
- Athanassoula, E., Lambert, J. C., & Dehnen, W. 2005, *Monthly Notices of the Royal Astronomical Society*, 363, 496
- Baldry, I. K., Glazebrook, K., Brinkmann, J., et al. 2004, *The Astrophysical Journal*, 600, 681
- Barden, M., Jahnke, K., & Häußler, B. 2008, *The Astrophysical Journal Supplement Series*, 175, 105
- Bell, E. F., Wolf, C., Meisenheimer, K., et al. 2004, *The Astrophysical Journal*, 608, 752
- Bernardi, M., Sheth, R. K., Annis, J., et al. 2003, *The Astronomical Journal*, 125, 1882
- Block, D. L., Buta, R., Knapen, J. H., et al. 2004, *The Astronomical Journal*, 128, 183

- Block, D. L., & Puerari, I. 1999, *Astronomy & Astrophysics*, 342, 627
- Block et al., D. 1994, *Astronomy & Astrophysics*, 288, 365
- Brinchmann, J., Charlot, S., White, S. D. M., et al. 2004, *Monthly Notices of the Royal Astronomical Society*, 351, 1151
- Bruzual & Charlot. 2003, *Monthly Notices of the Royal Astronomical Society*, 344, 1000
- Buta, R. J. 2013, 106
- Buta, R. J., Sheth, K., Regan, M., et al. 2010, *The Astrophysical Journal Supplement Series*, 190, 147
- Cardamone, C., Schawinski, K., Sarzi, M., et al. 2009, *Monthly Notices of the Royal Astronomical Society*, 399, 1191
- Cassata, P., Cimatti, A., Kurk, J., et al. 2008, *Astronomy and Astrophysics*, 483, L39
- Cheung, E., Trump, J. R., Athanassoula, E., et al. 2015, 13
- Cirasuolo, M., McLure, R. J., Dunlop, J. S., et al. 2007, *Monthly Notices of the Royal Astronomical Society*, 380, 585
- Conselice, C. J. 2003, *The Astrophysical Journal Supplement Series*, 147, 1
- . 2006, *Monthly Notices of the Royal Astronomical Society*, 373, 1389
- Cooray, A. 2005, *Monthly Notices of the Royal Astronomical Society*, 363, 337
- D. Block, R. W. 1991, *Nature*, 353, 48
- de Souza, R. E., Capelato, H. V., Arakaki, L., & Logullo, C. 1982, *The Astrophysical Journal*, 263, 557
- de Vaucouleurs, G. 1963, *The Astrophysical Journal Supplement Series*, 8, 31
- . 1991, *Third Reference Catalogue of Bright Galaxies*. (New York: Springer)
- Dieleman, S., Willett, K. W., & Dambre, J. 2015, *Monthly Notices of the Royal Astronomical Society*, 450, 1441

- Dressler, A. 1980, *The Astrophysical Journal*, 236, 351
- Eskridge, P. B., Frogel, J. A., Pogge, R. W., et al. 2000, *The Astronomical Journal*, 119, 536
- . 2002, *The Astrophysical Journal Supplement Series*, 143, 73
- Fillingham, S. P., Cooper, M. C., Pace, A. B., et al. 2016, arXiv:1606.07810
- Fortson, L., Masters, K., Nichol, R., et al. 2011, 11
- Franzetti, P., Scodéglio, M., Garilli, B., et al. 2007, *Astronomy and Astrophysics*, 465, 711
- Friedli, D., & Benz, W. 1993, *Astronomy and Astrophysics*, 268
- Fukugita, M., Nakamura, O., Okamura, S., et al. 2007, *The Astronomical Journal*, 134, 579
- Galloway, M. A., Willett, K. W., Fortson, L. F., et al. 2015, *Monthly Notices of the Royal Astronomical Society*, 448, 3442
- Giallongo, E., Salimbeni, S., Menci, N., et al. 2005, *The Astrophysical Journal*, 622, 116
- Graham, A. W., Driver, S. P., Petrosian, V., et al. 2005, arXiv:0504287
- Gunn, J., & E. and Gott, III, J. 1972, *apj*, 176, 1
- Hackwell, J., & Schweizer, F. 1983, *The Astrophysical Journal*, 265, 643
- Hart, R. E., Bamford, S. P., Willett, K. W., et al. 2016, *Monthly Notices of the Royal Astronomical Society*, 461, 3663
- Hawarden, T. G., Mountain, C. M., Leggett, S. K., & Puxley, P. J. 1986, *Monthly Notices of the Royal Astronomical Society*, 221, 41P
- Heckman, T., & Best, P. 2014, arXiv:1403.4620
- Ho, L. C., Filippenko, A. V., & Sargent, W. L. W. 1997, arXiv:9704100
- Hubble, E. 1926, *The Astrophysical Journal*, 64, 321

- Huertas-Company, M., Gravet, R., Cabrera-Vives, G., et al. 2015, The Astrophysical Journal Supplement Series, 221, 8
- Ilbert, O., McCracken, H. J., Le Fèvre, O., et al. 2013, Astronomy & Astrophysics, 556, A55
- Kawata, D., & Mulchaey, J. S. 2007, arXiv:0707.3814
- Knapen, J. H., Shlosman, I., & Peletier, R. F. 2000, The Astrophysical Journal, 529, 93
- Kormendy, J., & Kennicutt, R. C. 2004, Annual Review of Astronomy and Astrophysics, 42, 603
- Larson, R.B., Tinsley, B.M. and Caldwell, C. 1980, The Astrophysical Journal, 237, 692
- Lawrence, A., Warren, S. J., Almaini, O., et al. 2007, Monthly Notices of the Royal Astronomical Society, 379, 1599
- Lee, J., & Pen, U.-L. 2007, The Astrophysical Journal, 670, L1
- Lintott, C. J., Schawinski, K., Slosar, A., et al. 2008, Monthly Notices of the Royal Astronomical Society, 389, 1179
- Lintott, C. J., Schawinski, K., Keel, W., et al. 2009, Monthly Notices of the Royal Astronomical Society, 399, 129
- Martin, D. C., Fanson, J., Schiminovich, D., et al. 2005, The Astrophysical Journal, 619, L1
- Martin, D. C., Wyder, T. K., Schiminovich, D., et al. 2007, The Astrophysical Journal Supplement Series, 173, 342
- Martinet, L., & Friedli, D. 1997, Astronomy and Astrophysics, 323
- Masters, K. L., Mosleh, M., Romer, A. K., et al. 2010, Monthly Notices of the Royal Astronomical Society, 405, 783
- MenendezDelmestre, K., Sheth, K., Schinnerer, E., Jarrett, T. H., & Scoville, N. Z. 2007, The Astrophysical Journal, 657, 790

- Mignoli, M., Zamorani, G., Scudeggio, M., et al. 2009, *Astronomy and Astrophysics*, 493, 39
- Mulchaey, J. S., & Regan, M. W. 1997, *The Astrophysical Journal*, 482, L135
- Nair, P. B., & Abraham, R. G. 2010, *The Astrophysical Journal Supplement Series*, 186, 427
- Odewahn, S. C., Cohen, S. H., Windhorst, R. A., & Philip, N. S. 2002, *The Astrophysical Journal*, 568, 539
- Oh, S., Oh, K., & Yi, S. K. 2012, *The Astrophysical Journal Supplement Series*, 198, 4
- Peng, C. Y., Ho, L. C., Impey, C. D., & Rix, H.-W. 2002, *The Astronomical Journal*, 124, 266
- Peng, Y., Maiolino, R., & Cochrane, R. 2015, *Nature*, 521, 192
- Postman, M. Geller, M. 1984, *The Astrophysical Journal*, 281, 95
- Salim, S., Charlot, S., Rich, R. M., et al. 2005, *The Astrophysical Journal*, 619, L39
- Salim, S., Rich, R. M., Charlot, S., et al. 2007, *The Astrophysical Journal Supplement Series*, 173, 267
- Salimbeni, S., Giallongo, E., Menci, N., et al. 2008, *Astronomy and Astrophysics*, 477, 763
- Sandage, A. 1961, *The Hubble Atlas of Galaxies* (Washington: Carnegie Institution)
- Scarlata, C., Carollo, C. M., Lilly, S., et al. 2007, *The Astrophysical Journal Supplement Series*, 172, 406
- Schawinski, K., Thomas, D., Sarzi, M., et al. 2007, *Monthly Notices of the Royal Astronomical Society*, 382, 1415
- Schawinski, K., Lintott, C. J., Thomas, D., et al. 2009a, *The Astrophysical Journal*, 690, 1672

- Schawinski, K., Lintott, C., Thomas, D., et al. 2009b, Monthly Notices of the Royal Astronomical Society, 396, 818
- Schawinski, K., Urry, C. M., Virani, S., et al. 2010, 22
- Scoville et al., N. Z. 1988, The Astrophysical Journal Letters, 327, L61
- Seigar, M. S., & James, P. A. 1998, 11
- Sellwood, J. A., & Wilkinson, A. 1993, Reports on Progress in Physics, 56, 173
- Sheth, K., Regan, M. W., Scoville, N. Z., & Strubbe, L. E. 2003, The Astrophysical Journal, 592, L13
- Sheth, K., Vogel, S. N., Regan, M. W., Thornley, M. D., & Teuben, P. J. 2005, The Astrophysical Journal, 632, 217
- Sheth, K., Elmegreen, D. M., Elmegreen, B. G., et al. 2008, The Astrophysical Journal, 675, 1141
- Sheth, K., Regan, M., Hinz, J. L., et al. 2010, Publications of the Astronomical Society of the Pacific, 122, 1397
- Shlosman, I., Frank, J., & Begelman, M. C. 1989, Nature, 338, 45
- Simon, P., Hetterscheidt, M., Wolf, C., et al. 2009, Monthly Notices of the Royal Astronomical Society, 398, 807
- Skrutskie, M. F., Cutri, R. M., Stiening, R., et al. 2006, The Astronomical Journal, 131, 1163
- Steinhauser, D., Schindler, S., & Springel, V. 2016, arXiv:1604.05193
- Strateva, I., Ivezić, Ž., Knapp, G. R., et al. 2001, The Astronomical Journal, 122, 1861
- Strauss, M. A., Weinberg, D. H., Lupton, R. H., et al. 2002, The Astronomical Journal, 124, 1810
- Thronson et al., H. 1989, The Astrophysical Journal, 343, 158

- Tully, R.B., Mould, J.R., Aaronson, M. 1982, *The Astrophysical Journal*, 257, 527
- van Dokkum, P. G., Quadri, R., Marchesini, D., et al. 2006, *The Astrophysical Journal*, 638, L59
- Warren, S. J., Cross, N. J. G., Dye, S., et al. 2007, arXiv:0703037
- Whyte, L. F., Abraham, R. G., Merrifield, M. R., et al. 2002, *Monthly Notices of the Royal Astronomical Society*, 336, 1281
- Willett, K. W., Lintott, C. J., Bamford, S. P., et al. 2013, *Monthly Notices of the Royal Astronomical Society*, 435, 2835
- Wyder, T. K., Martin, D. C., Schiminovich, D., et al. 2007, arXiv:0706.3938
- Yang, G., Chen, C.-t. J., Vito, F., et al. 2017, *The Astrophysical Journal*
- Zhou, Z.-M., Cao, C., & Wu, H. 2014, *The Astronomical Journal*, 149, 1
- Zubovas, K., & Bourne, M. A. 2017, arXiv:1703.10782